MODIFICATION OF POROUS MATERIALS FOR VARIOUS APPLICATIONS

A Dissertation

by

ELIZABETH ANN JOSEPH

Submitted to the Office of Graduate and Professional Studies of
Texas A&M University
in partial fulfillment of the requirements for the degree of

DOCTOR OF PHILOSOPHY

Chair of Committee,	Hong-Cai Joe Zhou
Committee Members,	Marcetta Y. Darensbourg
	David C. Powers
	Jean-Philippe Pellois
Head of Department,	Simon W. North

August 2020

Major Subject: Chemistry

ABSTRACT

In recent years, there has been a rising interest in the field of highly-porous materials. Porous materials come in a large variety of subtypes, allowing for very high levels of versatility and tunability. Porous materials can include both organic and inorganic materials, such as polymers, mesoporous silica, zeolites, covalent organic frameworks (COFs) and metal-organic frameworks (MOFs). These materials often have varying pore sizes, beginning at the nano-scale and extending to visually discernable pore openings.

While a sizable portion of scientific research has focused on the development of novel porous materials with increasingly favorable properties, a significant portion of these porous materials have yet to find niche applications outside the laboratory. While many scientifically exciting discoveries perform admirably on the lab scale, going to bulk scale often comes with many challenges that do not present significant issues at smaller scales. Additionally, the syntheses of many porous materials, such as COFs and MOFs, are subject to very specific conditions, with minor changes in these procedures leading to an absence of product formation. As such, the work in this dissertation primarily focuses on materials with existing bulk production procedures, specifically discussing the modification of such materials to provide favorable properties that can then be applied to large scale production.

DEDICATION

To my grandparents, Danny, Angela and Gilbert, I wish you were here to see this.

To Danielle, Sherry and Grant, for my tenuous hold on sanity.

Finally, to the people who doubted, who gave me the drive to succeed.

ACKNOWLEDGEMENTS

I would like to thank my advisor, Dr. Zhou, and my committee members Dr. Darensbourg, Dr. Pellois and Dr. Powers, for their guidance and support throughout this arduous journey.

Thank you to my colleagues in Zhou group, for all the insightful discussions and for making my time in graduate school enjoyable. I would like to give special thanks to the following Zhou group members for their help and support, which has allowed me to be where I am today: Mathieu Bosch, who was always willing to discuss project ideas. Zachary Perry, for being the encyclopedia of knowledge I constantly turned to. Gregory Day, Sayan Banerjee, Angelo Kirchon and Hannah Drake, who were fantastic to work with on our many shared projects. Most importantly, to Carrie Fredricksen, without whom our group would have fallen apart.

This journey would not have been possible without the following people: Dr. Ozerov, for recruiting me to Texas A&M. Sandy and Valerie, for always being there for all of us. The wonderful people in the First Year Program, Dr. Lee, Dr. Bethel, Dr. Pellois, Dr. Altemose, Veronica, Kelley, Travis, Ken, and Dr. Clearfield, for making my teaching experience educational and enjoyable.

I would also like to thank my TAMU collaborator Ryan, a fellow graduate student in the Department of Chemical Engineering, and the beamline scientists at Lawrence Berkeley Labs: Simon and Laura, for their patience, trust and mentorship while working at the Small Molecule Crystallography Beamline.

None of this would have been possible without the two chemistry educators who came before, who inspired and encouraged my love for chemistry, leading to where I am today. To Mr. Kuo Yu-Hsuan, who I constantly pestered in class, thank you for feeding my curiosity where many others would not have, sparking my interest in chemistry. To Dr. So Cheuk Wai, my undergraduate research advisor, who took me under his wing and nurtured my self-confidence as a scientist and made our lab feel like a family, working together 8 days a week and keeping me from my day-of-the-week boyfriends. And to the many others who worked beside me in the labs I passed through, who made working enjoyable.

In addition to the individuals mentioned above, who have contributed to the completion of this degree in one way or another, there are a multitude of people I would like to acknowledge for their support throughout this journey, without which I would be a lot less sane.

Firstly, to my family, who have always been supportive of my foray into the sciences, provided me support and motivation to succeed and putting up with me moving halfway across the world.

To Hunter and his family, for the endless support and generosity.

To my friends in College Station: Mari, Quang, Jordon, Erick and Rachel, while each on our own personal journeys, the support and companionship has been a lifesaver.

To Tracy, Vivian, and all my friends back home, whose many milestones I have missed, while our meetings are few and far between, they are memories I will treasure.

Lastly, to TOTO, for the absolute bop that is Africa, which I listened to on loop while writing this dissertation.

And finally, in honor of Dr. Spencer Reid, “This is calm, and it’s Doctor.”

CONTRIBUTORS AND FUNDING SOURCES

Contributors

This work was supervised by a dissertation committee consisting of Professors Joe Zhou (Committee Chair), David Powers, and Marcetta Darensbourg of the Department of Chemistry and Professor Jean-Philippe Pellois of the Department of Biochemistry and Biophysics.

Preliminary testing for the work in Chapter 2 was conducted in part by Dr. Yu Fang of the Department of Chemistry and Ray Odzemir of *framergy*. High Pressure Volumetric Analysis (HPVA) testing was conducted by Sayan Banerjee and SEM images were taken by Carol Li of the Department of Chemistry.

The work in Chapter 3 was conducted in collaboration with Gregory Day, Hannah Drake, and Jeremy Willman of the Department of Chemistry. Infrared Spectroscopy in this chapter was provided by collaborator Kui Tan of University of Texas, Dallas.

The work in Chapter 4 was done in collaboration with Ruiqing Shen of the Department of Chemical Engineering, Texas A&M University.

All other work presented in this dissertation was completed by the student independently.

Funding Sources

Graduate study was largely supported by a teaching assistantship from Texas A&M.

This work was supported as part of the National Energy Technology Laboratory, funded under the U.S. Department of Energy Office of Fossil Energy under award #DE-FE0026825 (Porous Polymer Network Membranes with Porous Molecular Additives for Post-Combustion CO_2 Capture), Center for Gas Separations, an Energy Frontier Research Center funded by the U.S. Department of Energy, Office of Science, Basic Energy Sciences under Award # DESC0001015 (CO_2 separations and initial MOP studies), a National Science Foundation Small Business Innovation Research (NSF-SBIR) Grant #1632486 and the Robert A. Welch Foundation through a Welch Endowed Chair to H.J.Z. (A-0030).

The contents of this dissertation are not representative of the views of the above organizations.

NOMENCLATURE

3D	3-dimensional
ABTC	Azobenzenetetracarboxylic acid
BDC	Benzene Dicarboxylate
BET	Brunauer-Emmett-Teller
BJH	Barrett-Joyner Halenda
DFT	Density Functional Theory
DMF	Dimethylformamide
FID	Flame Ionization Detection
GC	Gas Chromatography
HPVA	High-Pressure Volumetric Analysis
IR	Infrared
MOF	Metal-Organic Framework
PCN	Porous Coordination Network
PMMA	Poly (Methyl Methacrylate)
PPN	Porous Polymer Network
PXRD	Powder X-Ray Diffraction
SEM	Scanning Electron Microscope
TGA	Thermogravimetric Analysis
UiO	University in Oslo

TABLE OF CONTENTS

Page

LIST OF FIGURES

Page

LIST OF TABLES

Page

CHAPTER I

INTRODUCTION

1.1 An Introduction to Porous Materials

There are many examples of porous materials observed in nature, one such example is a sponge. A sponge, like many porous materials, has clearly defined channels which allow for the flow of fluids through the bulk material. This concept serves as the basis for the analysis of porous materials.

While possessing a multitude of various properties, porous materials are, first and foremost, defined by their porosity, a characteristic that makes them a unique material class. Recently, MOFs have gained significant traction due to the properties that can be introduced with metal atoms[1], as well as their connecting organic ligands. Of the many existing porous materials, there are specific subclasses that have attracted a significant amount of attention, due to their chemical and physical properties. These include zeolites,[2] porous carbons,[3] mesoporous silicas,[1] metal-organic frameworks (MOFs),[4,5] covalent organic frameworks (COFs),[6] porous polymer networks (PPNs),[7,8] and gels.[9,10] In this dissertation, we will be focused on two main classes of porous materials, namely MOFs and PPNs.

When discussing porous materials, there are a few factors that need to be considered. These include their porosity, adsorption capability, durability, and ease of synthesis.[4,5] Additionally, the tailorability of porous materials and their properties has been a key factor in accelerating the research in this field. As there are many factors that culminate to give

the composition of porous materials, adjustments to each parameter allows for minor changes in both physical and chemical properties, resulting in an abundance of variations, each with unique applications.

1.2 Metal-Organic Frameworks (MOFs)

MOFs are currently at the forefront of materials research due to their unique compositions that allow for the generation of highly tuned structures with variable functionality, resulting in an expansive library of MOFs. While there are many other classes of porous materials that are being investigated by the scientific community, such as polymers, zeolites, and hydrogels, MOFs have proven to be some of the most versatile, with their wide tunability meaning that they can be engineered for a spectrum of applications.[5] MOFs are a hybrid porous material, composed of metal clusters, connected by organic linkers. They are often host to guest molecules, which occupy the pore voids within the framework. Some MOFs are unable to retain their structure when the guest molecules are evacuated, leading to structural collapse and the subsequent loss in porosity.

While MOFs offer a breakthrough in materials engineering, there are still challenges associated with MOF development, including low chemical and physical stabilities, complicated syntheses and difficulty in achieving commercial scale synthesis.[4,11] Over the years, many strategies have been developed to facilitate the tailoring of MOFs, which has resulted in the plethora of applications that can be found in the literature.

1.3 Porous Polymer Networks (PPNs)

PPNs are a class of organic material, synthesized through the formation of covalent bonds between monomers. The monomers used in the synthesis of these materials are often rigid in nature, forming an open structure, resulting in the material's defining features; high surface area and inherent porosity. However, PPNs can range significantly in crystallinity, from highly ordered crystalline materials (COFs), to materials that are mostly amorphous, with many varied states existing between these two extremes. As PPNs are synthesized via the formation of covalent bonds between organic linkers, they often have good physical and thermal stabilities, especially compared to MOFs, which often have labile metal-organic connections. As with most polymeric materials, the degree of polymerization can be controlled, and materials with varied properties can be synthesized using different synthetic conditions, resulting in a difference in physical properties. While polymeric materials have been intensively studied as a material class, the subclass of PPNs is still being explored. As more studies have been done to investigate the synthesis and properties of PPNs, there has been an accompanying resurgence in interest in porous polymer materials, focusing on rational, directed synthesis and design.

1.4 Characterizing Porous Materials

While porous materials do share many characteristics, when it comes to characterization, they can be separated into two main classes: crystalline and amorphous.

The defining feature of porous materials, porosity, can be measured through multiple methods. One of the most commonly used methods of determining porosity is the

application of Brunauer-Emmett-Teller (BET) theory. This theory aims to explain the mode of gas molecule adsorption onto solid surfaces and allows for the determination of a material's surface area. BET theory is an extension of Langmuir theory, which is applied to monolayer adsorption, whereas BET theory allows for the formation of multilayers. In BET analysis, one of the main features studied is the N_2 adsorption profile of a porous material.

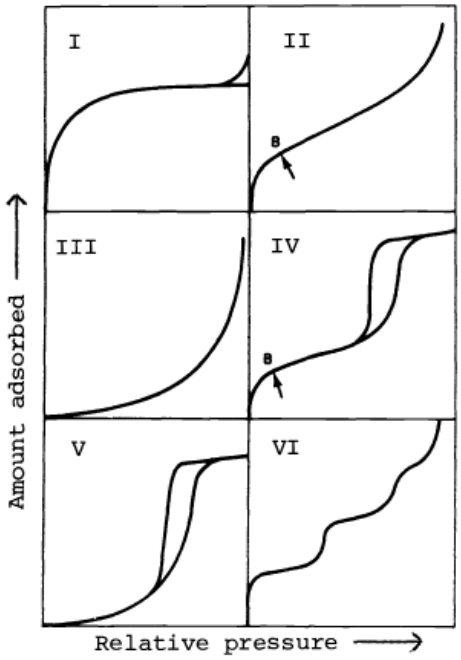

Figure 1. Isotherm Types as defined by IUPAC.[12]

As defined by IUPAC, there are six observed isotherm types.[12] The most commonly observed isotherms are the Type I and Type IV isotherms. Type I isotherms often demonstrate a rapid increase at low relative pressures, followed by a plateau, and are indicative of a microporous material, where the primary absorption occurs on the surface, as the small pore size limits the access to the internal porosity. Type IV isotherms possess

a characteristic hysteresis loop, which is indicative of capillary condensation, an artefact that is observed in the presence of mesopores. These isotherms also indicate the presence of multilayer absorption, occurring after the point B, indicated in Figure 1. Within the other isotherm types, Type II indicates a non-porous or microporous sorbent, Type III and V both indicate a material that experiences a stronger adsorbate-adsorbate interaction compared to adsorbate-adsorbent, with Type III often indicating non-porous materials and Type V indicating porous sorbents. Lastly, Type VI isotherms are observed in materials with multistep adsorption, with each step in the isotherm corresponding to a new phase of monolayer absorption.

While BET analysis is useful for the determination of surface area and pore size distribution, there are other methods of characterization that can provide us with more information regarding the material. In crystalline materials, we often look to X-ray diffraction to determine the exact structural arrangement of the atoms within the structure. Single crystal and powder X-ray diffraction (SCXRD and PXRD) are utilized in the characterization of crystalline porous materials, providing a wealth of information regarding the pore size, repeating unit, connectivity, and the structure of the secondary building unit. ‘

1.5 Applications of Existing Porous Materials

Given the usefulness of porous materials, there has been a significant surge in the development of new porous materials. Yet, upon closer inspection of commercial processes, it is clear that many of these innovative discoveries have yet to make the jump

from bench scale to commercial applications, demonstrating a need to bridge the gap, which can be achieved by further study of established, well-studied materials. The work in this dissertation focuses on taking existing porous materials that have been extensively studied and characterized and finding simple, low-cost modifications that can be applied to commercially available porous materials, providing a novel material that exhibits advantages over current state-of-the-art systems.

CHAPTER II

MODIFICATION OF PCN-250*

2.1 Methane Storage Using PCN-250

Natural gas, the principal ingredient of which is methane, can either be directly used as a fuel or processed into other energy resources.[13] Many energy-intensive solutions have been proposed to capture, store, and transport natural gas into the US energy infrastructure.[14] For example, natural gas can be successfully compressed to higher pressures up to 250 bar (3,600 psi), which is commonly referred to as compressed natural gas (CNG). It can also be liquefied at the temperatures less than @160°C, producing liquefied natural gas (LNG). These century-old technologies are known to improve the energy density of natural gas, to 9.2 MJL^{-1} for CNG or 22.2 MJL^{-1} for LNG respectively, but they are subsequently downgraded by about 30% volumetrically to account for their real cylindrical containment requirements.[15] In addition, both applications have intensive energy demands, creating critical cost issues. These issues have resulted in failure to fully utilize America's natural gas reserves.

Adsorbed natural gas (ANG) is an increasingly important method of improving natural gas storage.[16,17] In the past few decades, a variety of candidate absorbents, containing high surface areas, controlled pore diameters, and moderate binding energies, have been

*Part of the data in this chapter is reprinted and adapted with permission from "Incorporating Heavy Alkanes in Metal–Organic Frameworks for Optimizing Adsorbed Natural Gas Capacity" by Fang, Y.; Banerjee, S.; Joseph, E. A.; Day, G. S.; Bosch, M.; Li, J.; Wang, Q.; Drake, H.; Ozdemir, O. K.; Ornstein, J. M.; Wang, Y.; Lu, T.-B.; Zhou, H.-C., 2018. Chemistry A European Journal, 24, 16977-16982, Copyright WILEY 2018.

developed for research.[18] As a precisely tunable porous material, metal–organic frameworks (MOFs) have attracted great interest recently with their potential to boost ANG technologies.[19] Theoretical works suggested a conceptual MOF, IRMOF-993, could have a volumetric methane storage capacity well above activated carbon.[20] However, the MOFs in the study suffers from low chemical stability, especially in the presence of trace natural gas pollutants like hydrogen sulfide or water vapor.[21,22] Alternatively, an iron cluster-based MOF, PCN-250, is a radical departure from previously reported ANG MOFs due to its considerably higher stability. It is stable in boiling water as well as a wide range of pH conditions, maintaining its crystal structure and surface area. Moreover, PCN-250 exhibits a total reported methane storage capacity of 180 v(STP)/v, exhibiting a flat heat of adsorption curve, while also being capable of low-cost production.[23]

Here, we utilized a post-synthetic treatment of PCN-250 to obtain an enhanced, regenerable methane storage absorbent. The addition of a small portion of high boiling point alkanes into natural gas to increase the compression and/or refrigeration storage have been used for CNG and LNG for many years.[24,25] The alkanes not only increased the boiling point of the liquefied methane but also dissolved the hydrophobic methane through hydrophobic interactions.[26] Inspired by this idea, we incorporated C10 and C14 hydrocarbons into the pores of PCN-250 as a method of improving the ANG concept. We have dubbed the combination of methane absorption in high alkanes at high pressures, and its adsorption on the surface/pores of a porous material, HAANG (High Alkane Adsorbed Natural Gas).[27] The doped system allows for a higher volume of methane to be stored as

compared to the unmodified adsorbent at a given pressure. Most of the high alkane is also retained in and on the adsorbent through many working cycles of adsorption and desorption. This two-phase process, containing both liquid and vapor, can be achieved at suitable pressures (30–100 bar) and temperatures (260–323 K) for ANG technology.

2.2 Set Up for Testing Gravimetric Methane Uptake

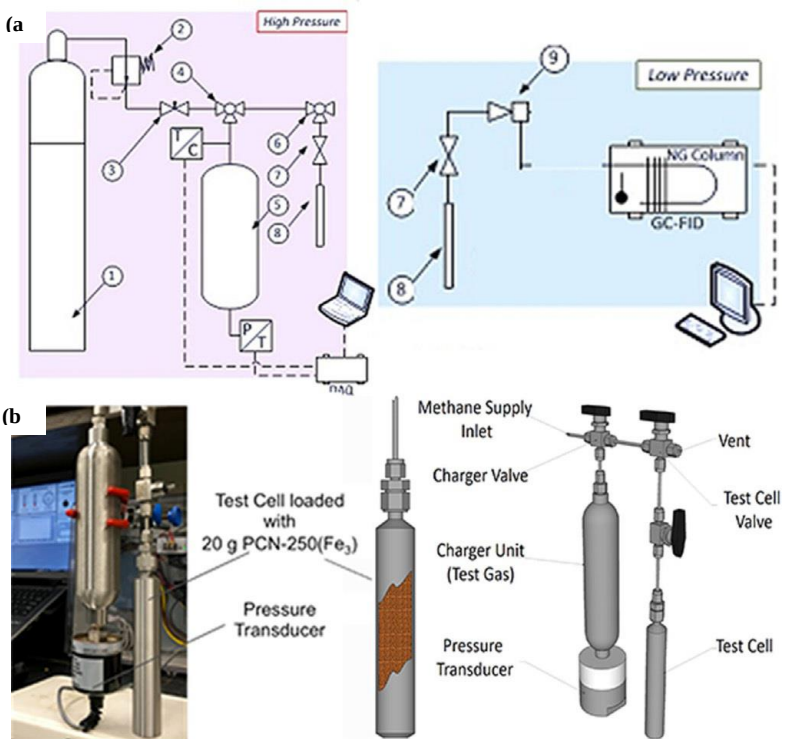

Figure 2a. Scheme of real-time gas adsorption/desorption monitoring station. (1: Test gas; 2: Pressure regulator; 3: Needle valve; 4: 3-way valve; 5: Test canister; 6: 3-way valve; 7: Ball valve; 8: Sorbent column; 9 :Ejector/Injector; T/V: Thermocouple; P/T: Pressure Transmitter; GC: Gas Chromatograph; FID: Flame Ionization Detector). **b.** A detailed demonstration of the charger unit (8: sample cell; 4, 6, 7: connections) monitoring station system. [98]

To realize the HAANG process, an apparatus was designed and constructed for direct volumetric measurement of methane uptake and delivery, as shown in Figure 2a. The

methane gas was first transported from the gas tank (Figure 2a, 1) to the charger unit (Figure 2a, 5). Then, the PCN-250 adsorbent (1 gram) was loaded into a test cell (Figure 2a, 8). By controlling the valves (Figure 2a, 4, 6 and 7), methane gas can be transported to the test cell and adsorbed by PCN-250. Due to the presence of a pressure transducer (Figure 2a, P/T) on the bottom of the charging unit, the final pressure (P_{fin}) can also be recorded. The initial pressure subjected to the methane supply inlet was assigned as P_{ini} (960 psi). By comparing the P_{ini} and P_{fin}, the adsorbed gas volume can be measured by the DP (P_{ini} - P_{fin}). Furthermore, the adsorbed gas in the test cell was discharged from the system and released into an airbag (1 L). A flow of atmospheric air was then injected into the airbag until it was full (1 L) to dilute the methane gas. A gas syringe was then used to inject 10 mL of the gas mixture into a gas chromatography-flame ionized detector (Figure 3a, GC-FID). Due to the deliverable methane being different for every experiment and the total volume of the airbag is a constant (1 L), the 10 mL in the syringe contains different amounts of methane. The injected methane gas was quantified by the integration area of the GC data. The integration area can represent the different ratio of deliverable methane in the air bag, thus the variation of deliverable methane can be analyzed. By using this system, it was found that PCN-250 can absorb and deliver an almost equal amount of methane gas repeatedly.

The methane uptake capacity of the alkane-doped PCN-250 samples (defined as Decane@PCN-250) were also measured with their methane uptake properties according to the above procedure. A sample of 1 gram of PCN-250 was filled in the test cell and

fully activated under vacuum at 160°C. Then the test cell was taken into an inert atmosphere (glove box) and 60 mL of n-decane was injected. After standing for 20 min, the test cell was sealed with 2 mm VCR gasket for the following gas test. Methane gas at 960 psi (66.2 bar) pressure was stored in the charger unit and then injected into the test cell.

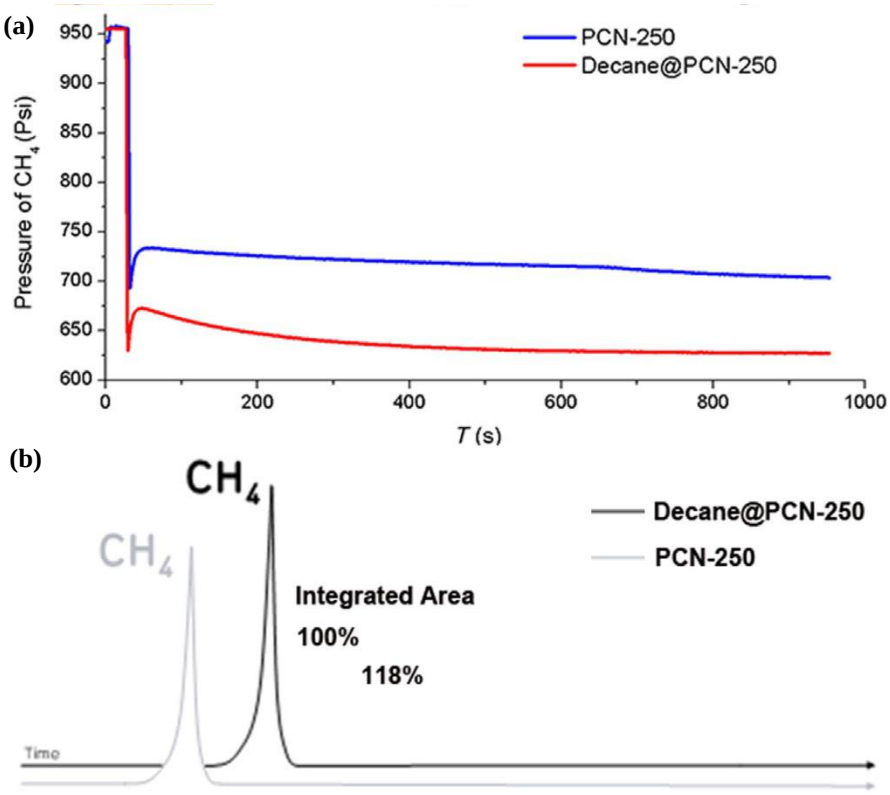

Figure 3a. Real-time monitoring of pressure drop of PCN-250 and PCN-250 doped with n-decane **b.** The GC-FID chromatogram showing the deliverable methane from PCN-250 and PCN-250 doped with n-decane. [98]

The pressure drop DP for the PCN-250 sample was 275 psi, which could be translated into adsorbed methane. Surprisingly, when PCN-250 was doped with n-decane, we found there was a dramatic increase of 21.8% for the DP (335 vs. 275 psi, Figure 3a). This suggests

that n-decane-doped PCN-250 has a storage capacity 21.8% greater than that of pristine PCN-250. Figure 3b shows a GC chromatogram comparing deliverable methane from PCN-250 at atmospheric pressure in the presence and absence of the doping agent (n-decane). Similarly, when PCN-250 was doped with n-decane, an 18.0% increase in the integrated area of the methane peak was observed. The pressure drop and GC results demonstrated an increase in total volumetric methane uptake of about 18% alongside the full desorption of methane, with the n-decane remaining in the PCN-250 adsorbent (not detectable by GC). It should be noted that the n-alkane loading was quite low (60 mL per 1 gram of adsorbent), accounting for 4.4 wt% of the MOF. When switched to a larger test tube filled with 20 grams of absorbent, a similar increase in methane uptake was observed. Not only PCN-250 but also other microporous and mesoporous MOFs were found to have similar increase in methane uptake when doped with different amounts and species of hydrocarbons (Figure 4-Figure 5Figure **6**).

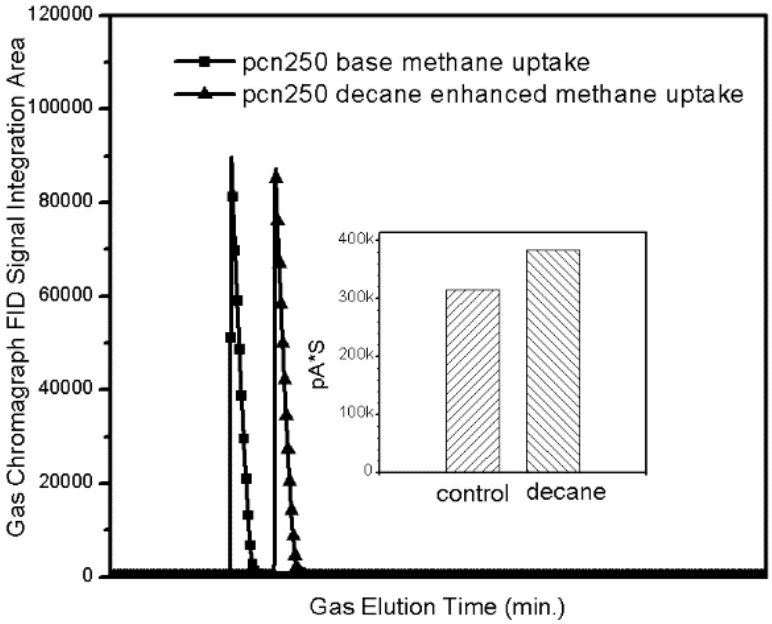

Figure 4. GC spectrum of methane adsorption observed in PCN-250 with and without n-decane doping. [98]

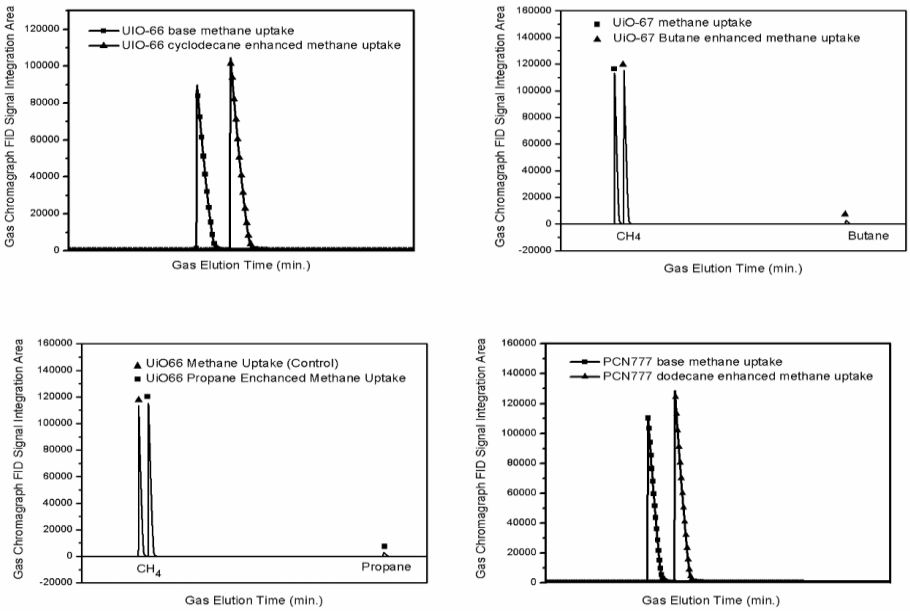

Figure 5 GC spectrum of methane adsorption observed in different MOF species with and without n-alkane doping. [98]

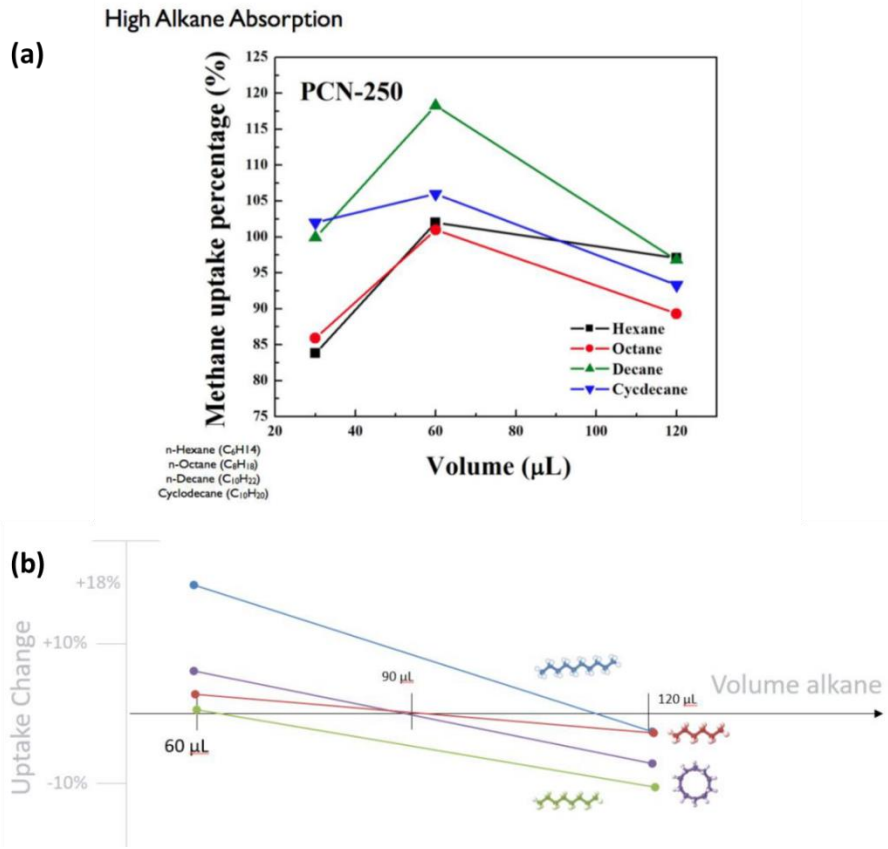

Figure 6a. Methane absorption capacity of PCN-250 at different alkane dopant levels **b.** Percent change in methane uptake with increasing alkane dopant. [98]

In addition, increasing the loading of *n*-decane with the MOF tended to result in decreasing methane storage capacity (Figure 6). Our hypothesis was that a large excess of *n*-decane would block the entrance of methane, thus inducing a decrease of methane uptake. As such, a method of developing larger pores in the structure was desired. Further screening of doping agents and engineering of the MOF–dopant interactions are needed to understand the system and demonstrate it as a proof-of-concept.

2.3 Introducing Mesoporosity in PCN-250

In order to improve the hydrocarbon loading in PCN-250, the generation of larger, mesoporous cavities was desired. In contrast with well-established methods of mesopore generation in MOFs, this method allows for pre-synthesized PCN-250 to be further treated to generate mesopores. Previously reported methods of mesopore generation have employed the use of MOFs that have inherent instability to specific conditions, such as hydrolysis. Herein, a well-known, microporous framework PCN-250, which comprises of an Fe-μ_3-oxo cluster and azobenzenetetracarboxylic acid (ABTC), and is also known as MIL-127 was used,[28,29] and the post-synthetic treatment resulted in the generation of mesopores within a primarily microporous structure. It is important to note that the key benefit of this methodology is that established MOF syntheses can be employed with no need for modification as the synthesis step does not affect the mesopore generation in the framework.

Traditionally, mesoporous MOFs are generated through extension of existing organic linkers, which results in a larger pore window. However, the synthesis of MOFs via this method has its limitations. Previous work by Yaghi et. Al. with the IRMOF series has demonstrated that the increase in linker length in an isoreticular series can be effective in growing new MOFs with larger pore windows.[30] However, longer linker lengths have also been shown to result in the growth of interpenetrated MOF networks. In interpenetrated MOF structures, the accessible surface area and pore volume are significantly decreased as the pore window is obstructed by the linkers of the interpenetrating species. Additionally, MOFs that are synthesized with longer linkers are often less robust due to

the increased flexibility of the linkers, with the decrease in rigidity often resulting in pore collapse upon the removal of guest molecules, significantly reducing the MOF's effectiveness.[31] Lastly, synthesis of large rigid linkers is often complex and requires a significant amount of time, money, or an extensive synthetic pathway, making it an impractical option at a large scale.

While large pore sizes and robustness are highly desired characteristics of MOFs, it is rare that these co-exist in the same framework as there is an inverse correlation between linker length and overall framework stability. Thus, it is essential that we develop a method of obtaining MOFs with good structural stability that can be used for the incorporation of large guest molecules.

While many frameworks are synthesized with inherent defects, there have also been many methods of generating desired defects in specific frameworks. Due to the drawbacks associated with isoreticular expansion, new pathways have been developed to synthesize MOFs with favorable pore sizes while retaining high structural integrity. Recent work done by Jiang and Cai demonstrated the use of a monocarboxylic acid as a modulator to generate hierarchically porous MOFs (HP-MOFs).[32] In this study, inherently microporous MOFs, such as UiO-66, were synthesized in the presence of fatty acids modulators. This resulted in metal clusters forming with fatty acids at the nodes, with the framework growing around these nodes. The steric bulk of these acids restricted the growth of the framework in this area. Following synthesis, the MOF was treated to remove the modulators, resulting in a mostly microporous framework with incorporated meso- or macropores. Further testing demonstrated that the HP-UiO-66 performed similarly to

unmodified UiO-66 when subjected to acidic and basic conditions, showing that tit maintained the stability of the microporous network, even with the presence of larger pores. Another recently reported work by Kim *et al.* demonstrated the hydrolytic generation of mesopores in a microporous framework.[33] Using a MOF that possesses poor water stability, large pores were generated by the partial removal of substituents in the framework through hydrolysis, with the structure going from a material with 2 sizes of micropores to one with 2 sizes of mesopores. While this method is simple and does not require specialty chemicals to execute, the method relies heavily on the framework's inherent instability to aqueous conditions. As such, while useful, this method is strictly limited to MOFs with water sensitive linkers.

Herein, we will discuss a novel methodology developed for introducing mesoporosity in a known microporous MOF, Additionally, PCN-250 can be commercially obtained through *framergy*™ and STREM chemicals, as AYRSORB™ F250.

2.4 Treatment of PCN-250 Material

Commercially available Fe-PCN-250, which was obtained from *framergy*™ was used as the standard test MOF due to the high availability of the material. PCN-250, also known as MIL-127, is a framework comprised of a trimeric metal cluster, formed by three Fe(III) octahedra sharing a central μ3-oxo, which is then linked by 6 ABTC ligands (ABTC = 3, 3‘, 5, 5‘-azobenzenetetracarboxylate) to form a soc net.[23] PCN-250 is known to possess good chemical and thermal stability, resisting degradation under temperatures up to 250°C in air, as well as being robust enough to withstand treatment in a wide range of aqueous

conditions. Previously established solvent exchange procedures involve the washing of PCN-250 with methanol, a highly volatile solvent, to remove the guest molecules that reside in the pore voids. Multiple solvent exchanges are required for the complete exchange of *N*,*N*-dimethylformamide (DMF) for methanol. This is typically conducted by drying the resultant MOF, followed by incubation with methanol in a sealed container in an 80 °C oven. Using this method, the microporosity of the MOF is retained, while the pores can be fully activated through high temperature vacuum activation with the removal of methanol. Initially, Soxhlet extraction was proposed as an alternative to multiple solvent exchanges, as the system allows for the continuous washing of the MOF with distilled solvent. However, upon further analysis, it was noted that the utilization of the Soxhlet methodology resulted in the consistent generation of a larger pore aperture.

Soxhlet washing was run on the material and the Brunauer-Emmett-Teller (BET) data was analyzed. It was noted that the N_2 uptake isotherms indicated that the two samples exhibited different pore character (Figure 7).

Pre-treated PCN-250 demonstrated a Type I isotherm, which is characteristic of microporous materials, while post-treated PCN-250 exhibited a noticeable step increase in adsorption at higher pressures, indicative of a Type IV isotherm. This Type IV isotherm is representative of a mesoporous material, as the large hysteresis is of a result of capillary condensation that occurs in the larger pore voids.

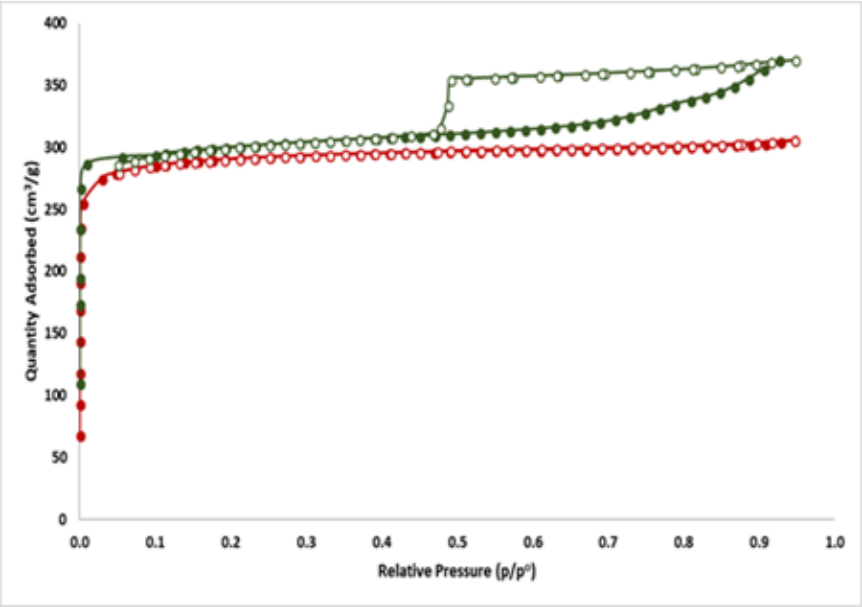

Figure 7 N_2 isotherms for post-treated (green) and pre-treated (red) samples of PCN-250.

Additionally, analysis of the pore size within the MOFs has shown an appearance of pores at 38 Å after treatment with methanol using the Soxhlet apparatus.

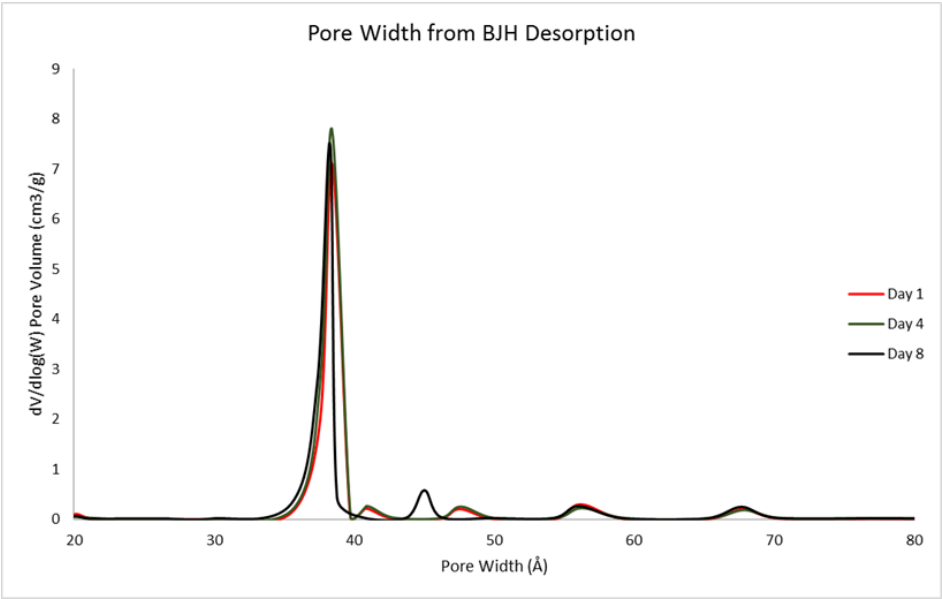

Figure 8. BJH Pore Size Distribution of Soxhlet Treated Samples demonstrating a peak at 38 Angstroms

Our initial hypothesis was that the hot solvent was simply removing residual starting material or synthesis solvent from the pores and that the mesopores observed were a result of defects present in the framework and were not directly resultant from the Soxhlet process. To test this hypothesis, samples of PCN-250 were washed using the typical bench method of multiple solvent exchanges with methanol in an oven. Comparison of the two materials led us to conclude that the as-synthesized material was inherently microporous, exhibiting the typical micropore size ca. 8 Å, and the larger pores were not generated without the use of the Soxhlet method. Additionally, it was noted that extended treatment using this method did not result in significant creation of pores of a larger size, or the overall degradation of particle size. An extended treatment over 12 days showed a generation of the 38 Å pore within the first day of treatment. Further treatment resulted in an increased proportion of mesopores generated but the majority of the pores were still of 38 Å in size. Additional testing was conducted with a larger scale set up, resulting in a similar generation of the 38 Å mesopore in the framework.

2.5. Micro- vs. Meso-porous PCN-250

Considering that n-decane (van der Waals diameter ~14 Å) is too large to be accommodated within the cavity of PCN-250 (pore size 8 Å), we hypothesized that it could be located within the mesoporous defects of the MOF. Thus, we introduced mesoporous defects into PCN-250 by Soxhlet treatment, to create mesoporous PCN-250 samples. The PCN-250 sample prepared according to reported literature is defined as

Micro-PCN-250. The Soxhlet treated sample, Meso-PCN-250, maintained the same crystalline morphology as Micro-PCN-250 (**Error! Reference source not found.**).

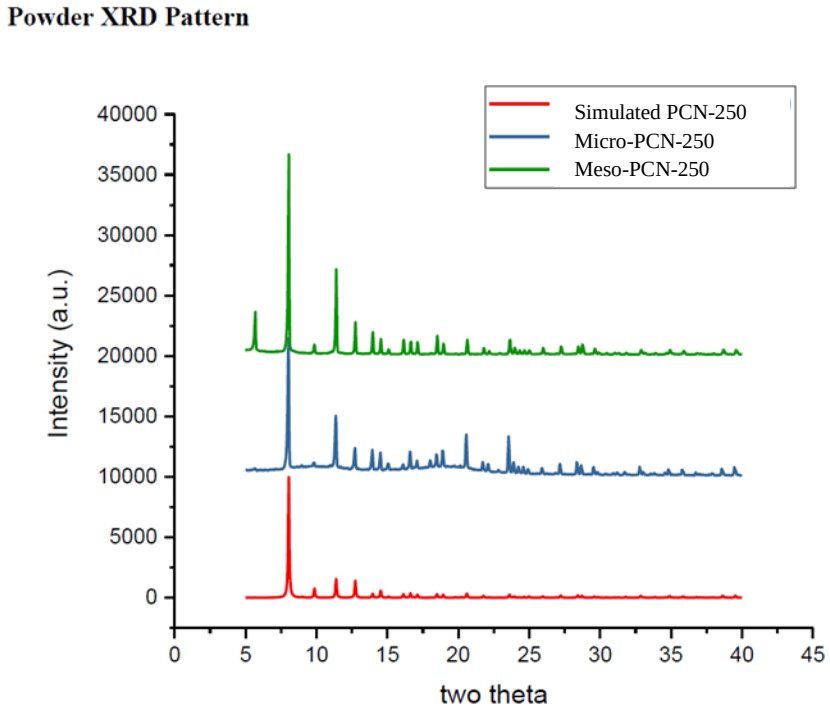

Figure 9. PXRD patterns of simulated, pre- and post-treated PCN-250, with no evident loss in crystallinity. [98]

However, high-resolution scanning electron microscopy (SEM) imaging clearly revealed that the mesoporous defects (about 3–5 nm) were generated at the surface of Meso-PCN-250 (Figure 10 b, d). The total N_2 uptake capacity of Meso-PCN-250 (398 cm^3g^{-1} STP) is largely similar to Micro-PCN-250 (405 cm^3g^{-1} STP). Notably, the N_2 adsorption-desorption isotherm (Figure 10 e, f) at 77 K clearly displays a type-IV isotherm with hysteresis loops characteristic of large constricted mesopores for Meso-PCN-250, providing evidence for Soxhlet induced mesopores within the framework.

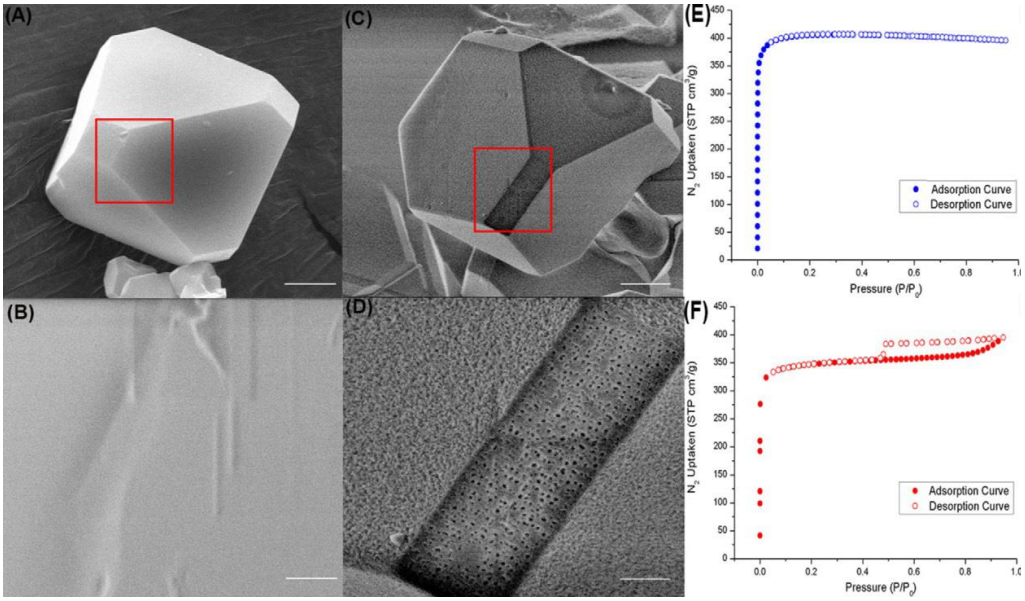

Figure 11. SEM image of **a.** Micro-PCN-250, **b.** Meso-PCN-250, scale bars for a-b: 1 micron, SEM image of indicated red area of **c.** Micro-PCN-250, **d.** Meso-PCN-250, scale bars for c-d: 200nm, **e-f.** N_2 isotherm of Micro- and Meso-PCN-250. [98]

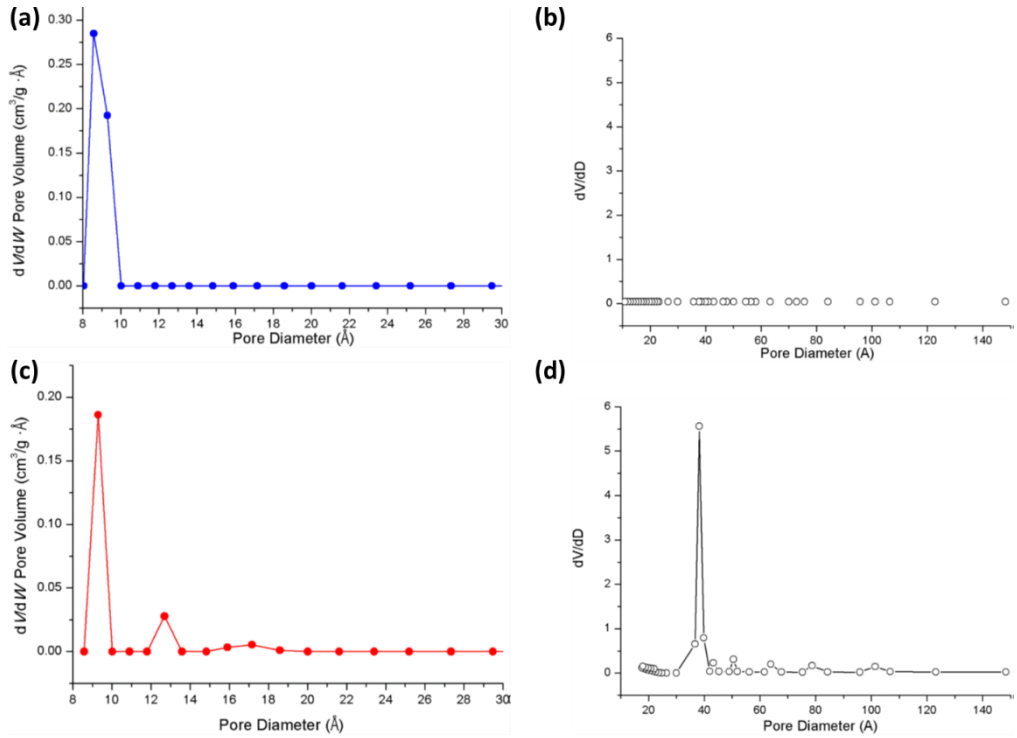

Figure 10. Pore size distributions **a.** Micro-PCN-250, DFT, **b.** Micro-PCN-250, BJH, **c.** Meso-PCN-250, DFT, **d.** Meso-PCN-250, BJH. [98]

The pore-size distribution (Figure 11d), as determined by the Barrett–Joyner–Halenda (BJH) desorption model, unambiguously shows that Meso-PCN-250 has ordered 3.8 nm mesopores, whereas Micro- PCN-250 does not (Figure 11b). By comparing the DFT-calculated pore volumes of the two samples, it suggests that the micropore volume decreased from 0.285 to 0.186 cm^3g^{-1} after mesopores were introduced to the PCN-250 samples (Figure 11a, c).

The high-pressure methane uptake of both PCN-250 adsorbents was measured at 298K using a Micromeritics HPVA-II (Figure 12). The Meso-PCN-250 has a methane uptake of 142 cm^3cm^{-3} at 65 bar, 11.8% lower than Micro-PCN-250 (161 cm^3cm^{-3}). It is well-known that mesoporous MOFs tend to have poor methane storage capabilities due to the large pore openings not being optimized for binding methane molecules.[34,35]

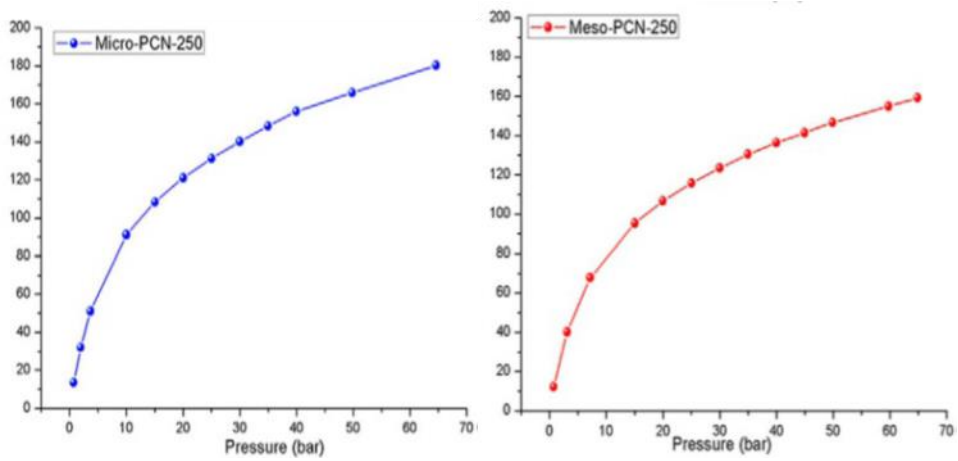

Figure 12. Methane uptake for Micro- and Meso-PCN-250 (without dopants). [98]

From the above characterization, we realized that Meso-PCN-250 maintains similar crystallinity and gas adsorption performance to Micro-PCN-250. However, Meso-PCN-250 exhibited a distinct pore-size distribution. The ordered and uniform mesopores of Meso-PCN-250 make it a suitable candidate for the investigation of hydrocarbon loading in PCN-250.

As the loaded alkanes investigated for the phenomenon tend to be in the gaseous or liquid phase and are easily desorbed, it is difficult to determine the actual loading within the MOF during tests. To prevent this ease of desorption, we opted to investigate fatty acid incorporation into MOFs. Considering that fatty acids are capable of coordinating with the metal cluster of the MOFs, which we hypothesized to have stronger binding to the MOF frameworks, as a result of the binding of the carboxylate groups to the metal clusters. Doped samples of n-decane and myristic acid, Decane@Meso-PCN-250 (4.4 wt% loaded) and Myristic@-Meso-PCN-250 (5.0 wt% loaded), were prepared accordingly. A PXRD of the doped absorbents showed a very similar pattern to that of as-synthesized PCN-250 and the simulated pattern (Figure 13a). The IR (infrared) spectrum (Figure 13b) of Myristic@Meso-PCN-250 shows a representative peak for myristic acid at 2800–2900 nm, indicative of successful binding of myristic acid to the MOF framework (Figure 14) .[36,37] As seen in Figure 13c, the thermal stability of samples before and after doping was analyzed by thermogravimetric analysis (TGA).

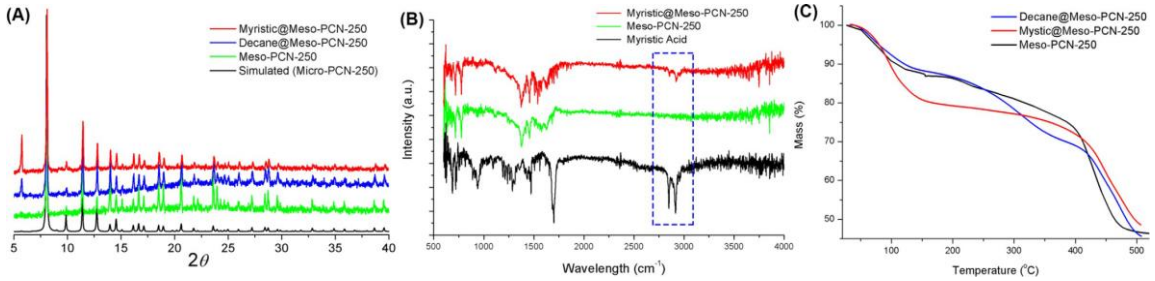

Figure 13a. Powder XRD pattern of Micro-, Meso-, Decane@Meso- and Myristic@Meso-PCN-250, **b.** FT-IR spectrum of Meso-, Myrstic@Meso-PCN-250, and Myristic Acid, **c.** TGA curve of Meso-, Decane@Meso- and Myristic@-Meso-PCN-250. [98]

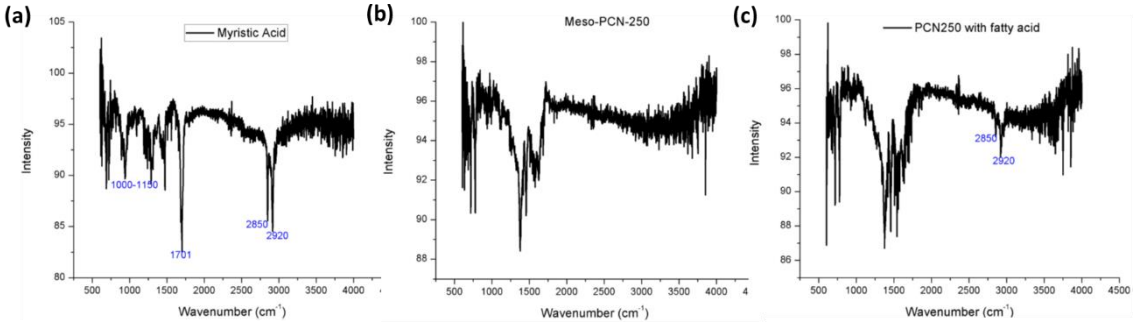

Figure 14. IR spectra of **a.** Myristic acid, **b.** Meso-PCN-250 and **c.** fatty acid doped Meso-PCN-250. [98]

The TGA curve of Meso-PCN-250 displays a mass loss of 5.6% below 100 °C, likely resulting from the removal of methanol from the framework. From 100–400 °C, the mass loss of Meso-PCN-250 is 17.0%, corresponding to the loss of residual guest DMF and other solvent molecules. The Decane@Meso-PCN-250 sample demonstrated a similar TGA curve, but with an additional weight loss step (12.1%) starting from 220 °C, which resulted from the loss of decane (boiling point of 174 °C). However, the TGA of Myristic@Meso-PCN-250 exhibited major differences when compared to the above two

samples in TGA. Below 150 °C, there is a significant mass loss of 19.2%, corresponding to the loss of methanol used in the loading of myristic acid (boiling point of 326 °C). In the range of 150–400 °C, the mass loss of Myristic@Meso-PCN-250 is only 7.3 %, which is the smallest of the three compared samples. This showcases the relatively slow desorption of myristic acid as compared to n-decane and DMF. There is also a slight shift in framework decomposition temperature in the Myristic@Meso- PCN-250, from 400 °C to 410 °C. This shift suggests that the incorporation of myristic acid into the MOF increases the thermal stability of the structure. After loading n-decane or myristic acid, the N_2 uptake of Meso-PCN-250 was considerably decreased (Figure 10f, Figure 15).

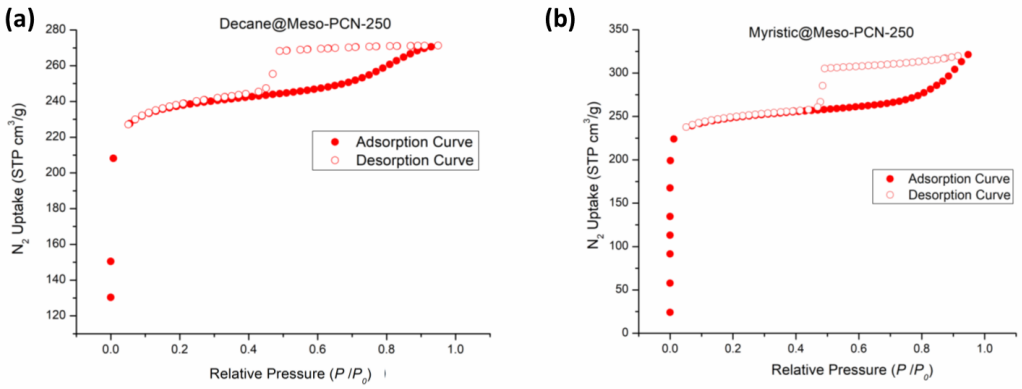

Figure 15. N_2 uptake of **a.** Decane@Meso-PCN-250 and **b.** Myristic@Meso-PCN-250. [98]

After doping with n-decane and myristic acid, both PCN-250 adsorbents were measured for high-pressure methane uptake at 298 K using the HPVA-II from Micromeritics (Figure 16).

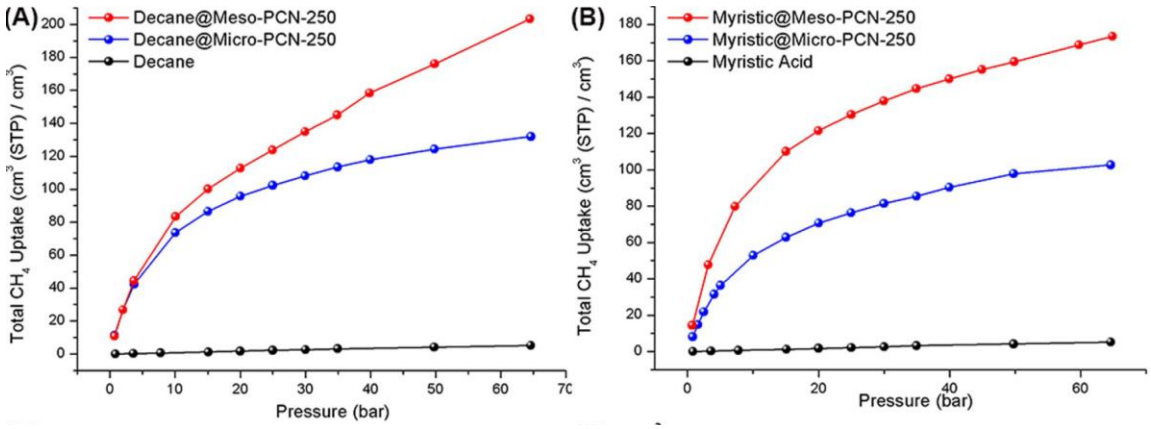

Figure 16. Volumetric total methane uptake of Micro-PCN-250 and Meso-PCN-250 doped with **a.** n-decane and **b.** myristic acid. [98]

The two doping reagents, n-decane, and myristic acid have minimal volumetric methane uptakes in the absence of the framework at 65 bar (10 cm^3cm^{-3} v/v). When Micro-PCN-250 was doped with n-decane and myristic acid, a decrease in methane uptake at 65 bar was observed (132 and 121 cm^3cm^{-3} v/v, respectively). Our simulated data also expressed the same trend as the experimental data obtained (Figure 17a, b).

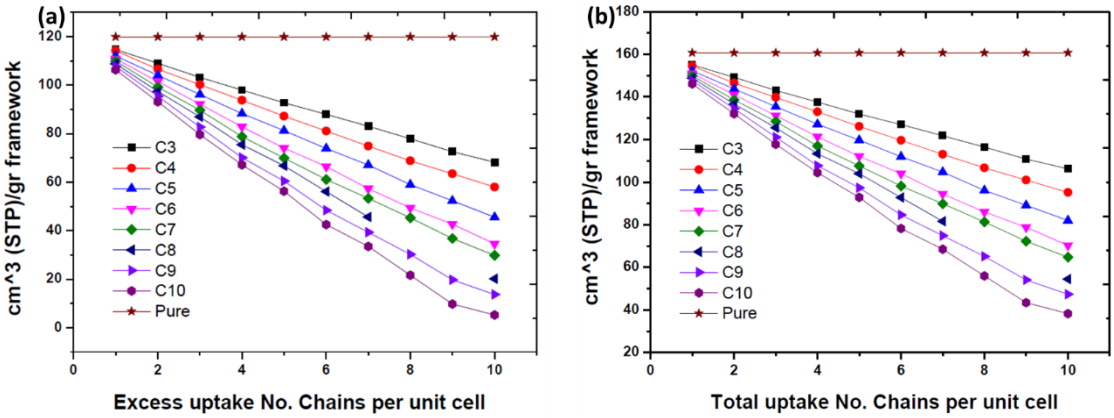

Figure 17a. Excess methane uptake and, **b.** Total methane uptake of microporous PCN-250 doped with hydrocarbons. [98]

In contrast, when Meso-PCN-250 was doped with n-decane, the methane uptake at 65 bar improved from 142 to 203 cm^3cm^{-3} v/v, which is a 43.0% increase compared to pristine Meso-PCN-250 (Figure 16a). When compared to the pristine Micro-PCN-250, the increased value is 26.1 %, which is comparable to the 18% increase for deliverable methane [characterized by GC-FID (Figure 3b)]. In addition, the working capacity (5–65 bar) of Decane@Meso-PCN-250 was also elevated, reaching 159 compared to 110 cm^3cm^{-3} v/v for Micro-PCN-250. Myristic@Meso-PCN-250 can reach a total methane uptake capacity of 173 cm^3cm^{-3} v/v at 65 bar (Figure 16b), and 192 cm^3cm^{-3} v/v at 95 bar (Figure 18).

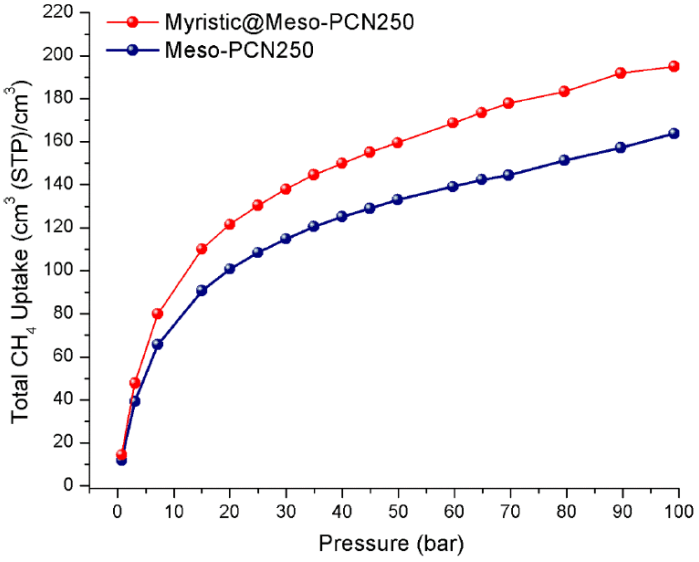

Figure 18. Total methane uptake of Myristic@Meso-PCN250 and Meso-PCN-250 samples (1-100 Bar). [98]

To the best of our knowledge, the 192–203 cm^3cm^{-3} v/v values represent record-high methane uptake of mesoporous PCN-250 adsorbents reported thus far.[23,38,39] It was also noted that the methane uptake increased faster for n-decane than that for myristic-acid-doped samples with increasing pressure (Figure 19). This can likely be ascribed to the stronger interactions between methane and high alkanes such as n-decane.[40,41]

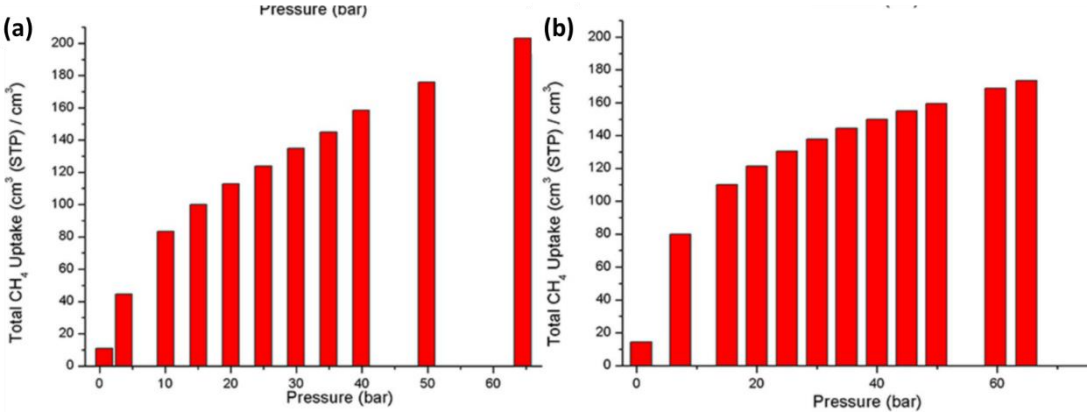

Figure 19. Total methane uptake of Meso-PCN-250 doped with **a.** n-decane and, **b.** myristic acid at each pressure. [98]

2.6 Recyclability of PCN-250 as a Methane Storage Material

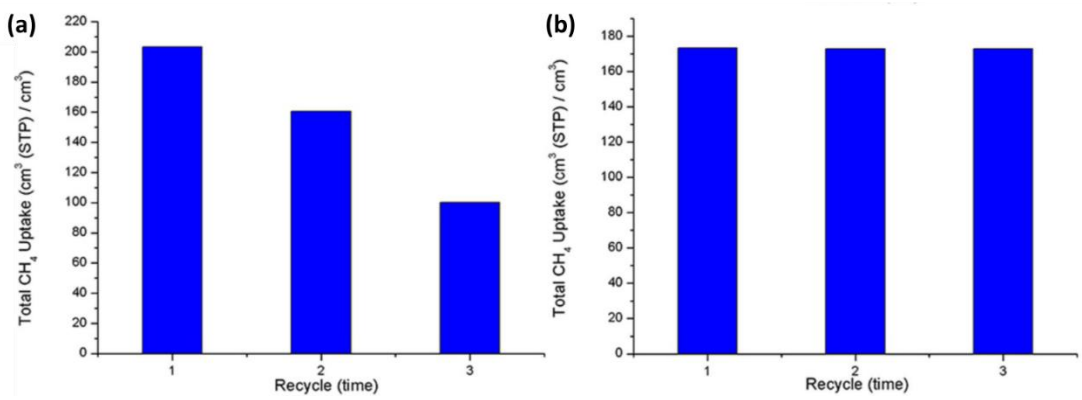

Figure 20. Recyclability tests for **a.** Decane@Meso-PCN-250 and, **b.** Myristic@Meso-PCN-250. [98]

Although n-decane doping has better methane adsorption performance than myristic acid doping, the recyclability follows the reverse trend (Figure 20). After three cycles, the performance of n-decane-doped samples was reduced to 50% of the initial cycle. Due to the lack of strong interactions between n-decane and the MOF, it is difficult to prevent the n-decane from leaching from the framework during the regeneration process, which included vacuum-assisted heating at 180 °C. After three cycles, the subsequent two cycles maintained a performance that was 45% that of the original. In contrast, myristic-acid-doped Meso-PCN-250 showed consistent performance even after three cycles. As expected, the carboxylic acid moieties of the fatty acid can bind to the metal cluster of the MOF adsorbent, reducing the loss of dopant during the desorption process.[42] The weight of myristic acid doped Meso-PCN-250 for each cycle was also measured, and no weight loss was found. This strongly indicated the retention of fatty acid within the framework throughout the gas storage cycle.

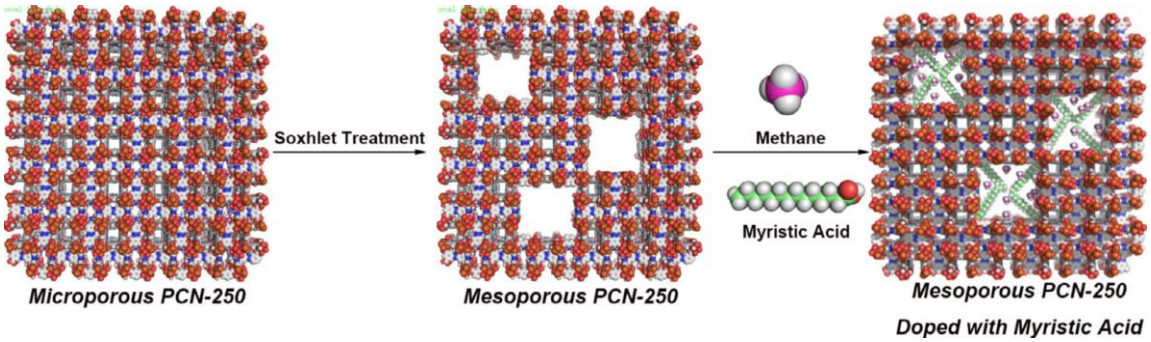

Figure 21. Illustration of myristic acid doped Mesoporous PCN-250 for methane uptake.[98]

According to the results obtained above, the proposed mechanism of the enhanced methane uptake by long chain hydrocarbon doped PCN-250 is illustrated in Figure 21. Through Soxhlet treatment, defects were created in the microporous PCN-250, yielding mesoporous PCN-250. Considering that mesopores have no significant interactions with small molecules, such as methane, methane uptake of undoped mesoporous PCN-250 was lower than that of undoped microporous PCN-250. In contrast, myristic acid strongly binds to the open metal sites of PCN-250, with long alkane chains located in the mesopores. By taking advantage of hydrophobic interactions and efficient space partition, methane molecules were packed into the mesopores, resulting in enhanced uptake capability. Although there are several pre- or post-synthetic methods to introduce mesoporous defects in MOFs, it is very rare that a MOF shows increased methane uptake after the treatment.[32,43–47] Furthermore, compared to conventional methods previously reported, the HAANG method can produce enhanced methane storage and is more straightforward and more highly recyclable.

2.7 Conclusion

In conclusion, we applied a post-synthetic treatment method, termed HAANG, to MOF adsorbents and obtained MOF-hydrocarbon composites with improved methane uptake performance and excellent recyclability. By applying two forms of the same MOF, microporous and mesoporous PCN-250, we observed that doping reagents only improve the methane uptake performance for Meso-PCN-250 and reduce the performance for Micro-PCN-250. This result indicates that the doping reagents are presumably located

within the mesopores or at defect sites in the adsorbent, utilizing the void space and dissolving additional methane molecules. Through doping weakly (n-decane) and strongly (myristic acid) binding agents, the Meso-PCN-250 can produce a robust reusable adsorbent composite with increased methane uptake performance. Our findings shed light on the potential for post-synthetic treatment of MOF absorbents to obtain high performing and sustainable natural gas resources.

2.8 Experimental

Powder X-ray diffraction (PXRD) was carried out with a Bruker D8-Focus Bragg-Brentano Xray Powder Diffractometer equipped with a Cu sealed tube (λ = 1.54178 Å) at 40 kV and 40 mA. N_2 sorption measurements were conducted using a Micromeritics ASAP 2020 and 2420 system. All BET samples were activated at 185 °C for 12 hrs.

2.8.1 Micro-PCN 250 Synthesis

$Fe(NO_3)_3 \cdot 9H_2O$ (5.4 g), ABTC (1.8 g), Acetic Acid (3 L) and DMF (6 L) were added into a jacketed 10 L Pyrex high pressure reaction vessel. The vessel was then heated to 150 ºC for 12 h. The resulting reaction slurry was then removed and used without further purification.

2.8.2 Washing Procedure for PCN-250

PCN-250 and methanol were added to a vial in an approximate 1:3 volume ratio. The mixture was incubated in an 80C oven overnight. The material was cooled and filtered. This was repeated three times to allow for complete solvent exchange and removal of residual contaminants.

2.8.3 Initial Slow Drip Test

PCN-250 was washed in a Soxhlet setup with refluxing methanol. 0.5g samples of PCN-250 were packed into individual filter paper pockets as demonstrated in Figure X. 8 total samples were placed into the Soxhlet apparatus at the same height. Methanol was added to the solvent reservoir and heated to reflux, with an approximate drip rate of 12 drops/min. Samples were then removed from the set up at regular intervals. BET N_2 sorption analysis and PXRD were run.

2.8.4 Initial Fast Drip Test

PCN-250 was washed in a Soxhlet setup with refluxing methanol. 0.5g samples of PCN-250 were packed into individual filter paper pockets as demonstrated in Figure X. 10 total samples were placed into the Soxhlet apparatus at the same height. Methanol was added to the solvent reservoir and heated to reflux, with an approximate drip rate of 170 drops/min. Samples were then removed from the set up at regular intervals. BET N_2 sorption analysis and PXRD were run.

2.8.5 Bulk Fast Drip Time Test

PCN-250 was washed in a Soxhlet setup with refluxing methanol. 5.00g of PCN-250 was packed into a cellulose sleeve for Soxhlet extraction. Methanol was added to the solvent reservoir and heated to reflux, with an approximate drip rate of 170 drops/min. The sample was left to run for 6 days. BET N_2 sorption analysis and PXRD were run.

2.8.6 Bulk Fast Drip Time Test 2

PCN-250 was washed in a home-built Soxhlet setup with refluxing methanol. Approximately 30.00g of PCN-250 was placed into a fine fritted tube for Soxhlet

extraction. Methanol was added to the solvent reservoir and heated to reflux. The samples were taken at 5, 8 and 11 days. BET N_2 sorption analysis and PXRD were run.

2.8.7 Fatty Acid Loading of PCN-250

A series of fatty acids (C6 to C14) were loaded into PCN-250 using the following procedure. 1.00g of mesoporous PCN-250 was added to a vial. 0.2 mass equivalence, 200mg, of fatty acid was weighed into the same vial, followed by 10ml of methanol. The resulting mixture was incubated in a 75 °C oven overnight. The material was filtered and allowed to dry in a 75 °C oven overnight. Samples of C12 and C14 were prepared with varying weights due to sample limitations, but the mass ratio and solvent volume ratios were maintained.

2.8.8 Myristic Acid Loading Screen

Myristic acid was added to a vial containing 1.00g of untreated PCN-250 at various loadings 0.05, 0.1, 0.25, 0.5 and 0.75 mass equivalence. 10 ml of methanol was added to each sample vial. The vials were sealed and incubated in an 80 °C oven for 3 days. An identical test was set up with samples of mesoporous PCN-250.

CHAPTER III

PPN-150: A MELAMINE-FORMALDEHYDE POLYMER NETWORK*

3.1 Carbon Capture in the United States

Global warming has become an imminent environmental threat, with climate change being considered a contributing factor for the increase in frequency and severity of inclement weather,[48] potentially resulting in negative health effects through preventing access to health services,[49] as well as hurting the global economy through expensive weather remediation[50]. One of the main gases of concern, CO_2, is mainly sourced through the burning of fossil fuels and has experienced an exponential increase in atmospheric concentration since the 1800s.[51] In particular, fossil fuels account for 63% of the energy generated in the United States.[52] With fossil fuel reserves expected to last well past 2050,[53] finding new methods of CO_2 remediation is of the utmost importance to mitigate the effects of global warming.

Many approaches to CO_2 capture have focused on post-combustion capture or capture directly downstream from fossil fuel power generation. Post-combustion flue gas is typically comprised of ~12–15% CO_2 and 74–80% N_2, with the remainder consisting of ppm levels of SOx, NOx, particulate matter, H_2O, and O_2. Currently, mature post-

* Parts of this chapter are reprinted and adapted with permission from "Day, G. S., Drake, H. F., Joseph, E. A., Bosch, M., Tan, K., Willman, J. A., Carretier, V., Perry, Z., Burtner, W., Banerjee, S., Ozdemir, O. K., Zhou, H.-C., Improving Alkylamine Incorporation in Porous Polymer Networks through Dopant Incorporation. Advanced Sustainable Systems, 2019, 3, 1900051." Copyright WILEY 2019

combustion CO_2 capture processes utilize amine solutions, most notably 30% aqueous monoethanolamine (MEA) .[54] However, aqueous MEA solutions tend to have regenerative energy demands of up to 185 kJ mol^{-1} CO_2. Recovering the CO_2 and regenerating the sorbent can cause a drastic increase in the parasitic load of the system, oftentimes upward of 70%.[55]

3.2 Materials for Carbon Capture

In order to reduce the energy demand of these solution-based systems, there has been a renewed effort toward the development of solid sorbents for CO_2 capture. Solid sorbents are advantageous as they capture CO_2 through physisorption, which does not entail the generation of full sorbent–amine bonds such as in the chemisorption-based capture of aqueous amine solutions. A number of different classes of solid sorbent have been investigated, such as metal–organic frameworks (MOFs) ,[56,57] mesoporous silicas, [58,59]zeolites,[60,61] and porous polymers.[62,63] Solid sorbents demonstrate a number of advantages over their amine solution counterparts. The typical heats of adsorption for amine solutions range from 80 to 185 kJ mol^{-1} CO_2,[55,64] whereas solid sorbents can have both broader and lower ranges for heats of adsorption from 30 to 90 kJ mol^{-1} CO_2. This variability depends on the available functional groups within the structure.[56,61,65]

Purely physisorptive materials are often inadequate for CO_2 capture due to their low gas selectivity. As a result, there has been a push toward improving these solid sorbents through the incorporation of chemisorption functionalities. Typically, these improvements in capture capabilities directly result from the introduction of amine functionality within

the porous materials. This incorporation can be through post-synthetic covalent tethering,[56,57,66] physical incorporation,[59,67] or direct incorporation into the porous framework scaffold.[62,63,68]

Physical incorporation of amines within porous materials remains one of the more feasible methods of improving their CO_2 affinity. The low cost associated with physical incorporation-based procedures typically requires little more than the short-term contact between the porous material and a suitable amine. However, the weak physisorptive tethering of the amine to the surface of the porous material limits the conditions under which the material can be used. The amine leaching that can occur during sorbent regeneration results in a loss of CO_2 uptake performance capacity and leads to concerns over equipment corrosion and environmental exposure to toxic chemicals.

As an organic species, PPNs are ideally suited for functionalization, taking advantage of multiple organic synthetic pathways,[66] while still being producible at low cost.[69,70] PPNs incorporated with basic moieties, such as amines, can produce high CO_2 selectivities, necessary to separate CO_2 from flue gas.[66,69,70] The incorporation of amines into a PPN system is typically achieved through either post-synthetic modification of an existing porous polymer,[66] or the incorporation of basic moieties into the polymer backbone.[62,63,68] Previous results from our lab have shown high uptake capacities using both PPN-6 and PPN-125,[66,69] both being porous networks post-synthetically modified with covalent diethylenetriamine tethering. However, in both systems the addition of covalently tethered amine adds two steps to the sorbent synthesis. With processing adding additional days to the total sorbent reaction time and adding to the amount of required solvents and reagents,

this increases the total cost of the synthetic process. The preparation of PPNs with basic moieties incorporated directly into the polymer backbone shows CO_2 uptakes greater than 10%wt only when adsorption is conducted at sub-ambient conditions. This limitation reduces the usefulness of these sorbents for industrial scale capture.

To combat these issues, we have introduced dopant materials: functionalized small molecules that can be added during PPN formation. The dopants utilize hydrogen bonding and strong dipole–dipole interactions to act as noncovalent anchoring sites for the post-synthetically loaded alkylamines. This dopant system represents a distinct advantage over other physisorptive systems as it can achieve the high CO_2 cycling capacity necessary for an industrially relevant sorbent, while maintaining a high degree of cyclability.

3.3 Results and Analysis

The mPMF backbone of PPN-150 was chosen as a scaffold due to its ability to form a highly porous framework using commercially available materials (melamine and formaldehyde). However, melamine-formaldehyde resins are not inherently porous, and therefore must be made porous through the precise control of the synthetic procedure. The production of PPN-150 proceeded through a condensation polymerization of melamine and formaldehyde (in the form of paraformaldehyde) at high temperatures (150–170 °C) in dimethyl sulfoxide (DMSO) solution without stirring. Upon sitting for ~1 hour, an initial polymer gel formed. This gel is a soft pliable material that collapses in the absence of solvent. Upon being left in the sealed container under an atmosphere of formaldehyde gas for 3 to 7 days, the gel slowly solidified into the thermoset melamine-formaldehyde

resin. The resulting polymer monolith was then crushed into useable sized pieces and washed with acetone, tetrahydrofuran, dichloromethane, and methanol successively. The three main parameters that affected the porosity in PPN-150 were: the fill volume of the container used for synthesis, the solvent used for synthesis, and the reaction time.

Table 1. Reactor Headspace Optimization (PPN-150)

Reactor fill volume (%)	**BET Surface Area (m^2g^{-1})**	**Pore volume (cm^3g^{-1})**
18.3	857	0.685
50.0	838	0.886
88.4	722	0.802

There is a mild correlation between the first two parameters as it appears that the concentration of formaldehyde gas in the reaction solution versus in the headspace of the material can result in a change in the surface area and pore volume of the resultant sample. As a result, both the vapor pressure of the formaldehyde and the solvent play an important role in determining the degree of micro and mesoporosity as well as the surface area of the material. The results of the synthetic tests (Table 1) show that container fill volume, defined as the volume of the container filled by the reaction solution, does have a minor effect on the overall porosity of the samples. Reaction vessels that had a higher percentage of their volume filled resulted in polymer with lower Brunauer–Emmett–Teller (BET) surface areas. The reaction vessel that was only 18.3% full results in a PPN that had an 18.7% higher surface area compared to a sample that was produced in an 88.4% filled vessel.

Table 2. Solvent System Optimization Data for PPN-150

Solvent System	**BET Surface Area (m^2g^{-1})**	**Pore volume (cm^3g^{-1})**
Dimethyl Sulfoxide	854	1.11
Ethylene Glycol	356	0.761
Ethylene Glycol/Ethanol	251	0.542
Dimethyl Sulfoxide/Water	113	0.135
Ethylene Glycol/Water	298	0.653
Ethylene Glycol/ Methanol	279	0.597
Dimethyl Sulfoxide/Methanol	518	0.508

Solvent comparisons were conducted in an attempt to produce PPN-150 using greener, more environmentally friendly solvents. These solvent choices were compared to DMSO, the solvent commonly used in the literature for mPMFs.[70] Unfortunately, no other solvent or solvent pairs came close to the high surface area or porosity of the DMSO synthesized sample (Table 2).

Table 3. Time Optimization for PPN-150

Synthesis Time (Days)	**BET Surface Area (m^2g^{-1})**	**Pore Volume (cm^3g^{-1})**	**TGA CO_2 Uptake (wt% DETA loaded)**
3	730	0.296	9.6
5	640	0.281	9.2
7	1014	1.042	5.3

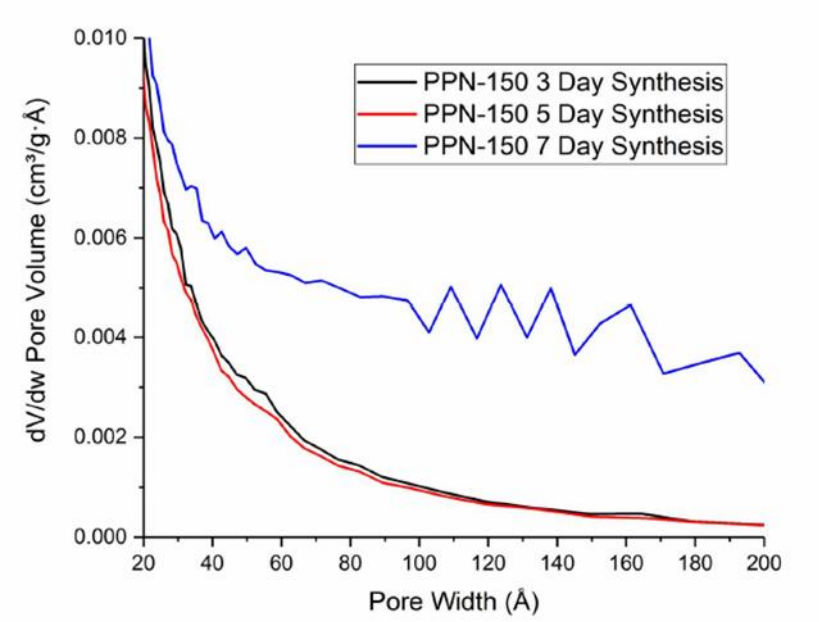

Figure 22. Pore size distribution change for time optimization study of PPN-150. [99]

Reaction time analysis shows a distinct change in sample porosity as the reaction continues (Table 3). In general, there appears to be an increase in overall porosity as the reaction progresses. However, changes in the pore size distribution (Figure 22) suggest that the increased porosity is mainly generated in the higher mesoporous range. Unfortunately, the mesoporous range is less relevant when investigating CO_2 capture after alkylamine loading (Table 3).

Table 4. Elemental Analysis of PPN-150 Series Samples

Element	**C**	**H**	**N**	**S**
Theoretical Mass% for PPN-150	34.00	2.00	45.00	0.00
Experimental PPN-150	35.26	4.83	40.89	5.81
Experimental PPN-151	35.23	5.28	39.45	5.88
Experimental PPN-152	36.81	4.91	40.56	5.80
Experimental PPN-153	36.68	5.33	36.47	7.21
Experimental PPN-154	34.75	5.27	35.92	7.13
Experimental PPN-155	36.07	5.45	37.99	5.06
Experimental PPN-156	33.84	5.37	41.12	3.78

DMSO is known for having both a high boiling point and for decomposing near its boiling point into dimethyl sulfide, which could potentially interfere with the PPN reaction. Elemental analysis of the processed PPN-150 shows that the material is still 5.81% sulfur by mass (

Table 4), suggesting that DMSO lingers in the sample, even after processing. However, heating the starting materials of the PPN in the absence of formaldehyde in DMSO shows no observable reaction.

CO_2 uptake testing of lab-scale PPN-150 samples was conducted using thermogravimetric analysis (TGA) and showed an uptake of 2.8 wt% under simulated flue gas conditions (0.15 bar CO_2, 0.85 bar N_2). Alkylamines were then incorporated into the polymer pores, taking advantage of the basic moieties in the alkylamines to engage in a weak chemisorptive interaction with CO_2. Loaded tests were performed using PPN-150 samples with a high surface area, produced in an 18.3% filled reactor using DMSO as a solvent, with a series of alkylamines. The alkylamines were doped into the polymer by mixing the solid PPN in a solvent, typically hexane, cyclohexane, or methanol, and adding the neat alkylamine to the solution. The alkylamine was allowed to penetrate the PPN with the aid of a sonication bath at 50 °C over the course of 3 h. The PPN was then filtered, washed with a polar solvent (THF, methanol) in an attempt to remove surface alkylamines, and then dried in a vacuum oven at 85 °C for 1 h. The resulting white powder samples were then tested for CO_2 uptake under TGA conditions and run for five cycles (Figure 23).

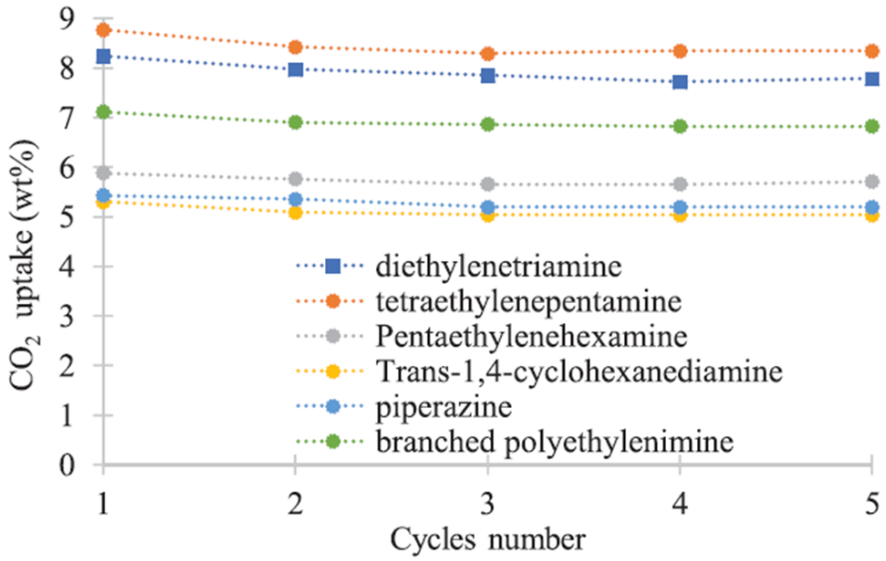

Figure 23. Testing of different amines loaded into PPN-150 over 5 cycles.[99]

Based on the data gathered, the two highest performing alkylamines were diethylenetriamine (DETA) and tetraethylenepentamine (TEPA). However, in an effort to keep synthesis costs down, and due to the uptake values of the two materials being relatively close (both achieved >8% on a typical CO_2 capture experiment), we decided to focus our research efforts on the DETA loaded PPN.

During TGA cycling, it was observed that there was still a loss of uptake performance over the five cycle experiment. This was attributed to the loss of amine due to thermal regeneration. This loss is likely due to the main nitrogen component of the PPN, the triazine ring, only being weakly basic. This could be corroborated by the loss of sorbent mass between cycles. In order to alter the structure of the PPN, we opted to try dopant

incorporation, adding functional molecules during the polymerization reaction, as a method of either altering the structure through templating and changing the porosity, or by adding secondary sites for amine tethering to occur. Further work by another researcher was conducted regarding templating using other moieties was conducted separately, investigating the six dopants as shown in Figure 24. The six dopants were added to the polymer before the initial gel formation, with the dopants added as a DMSO solution to a hot melamine solution prior to the addition of paraformaldehyde. The reaction temperature and conditions used were the same as for the base polymer, PPN-150.

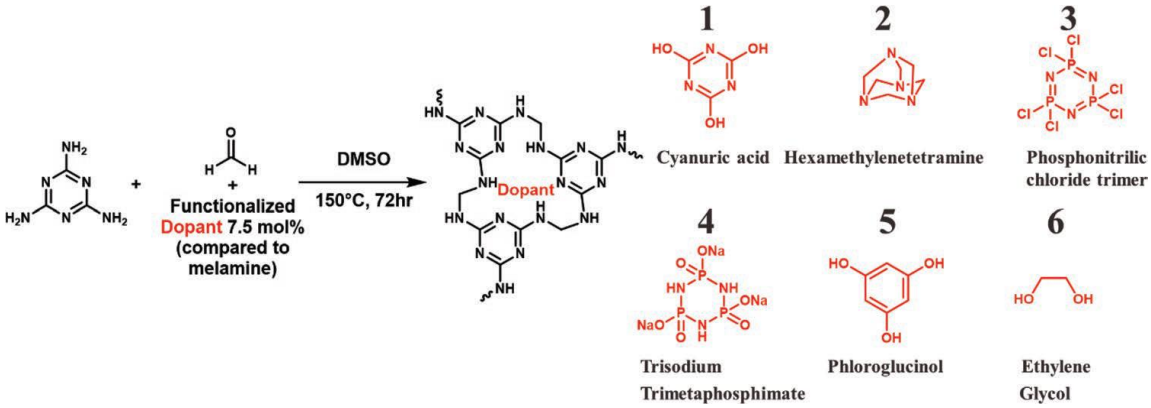

Figure 24 Procedure for the synthesis of doped PPN-150 series polymers. Dopants (1-6) were added to the initial reaction mixture and homogenized prior to polymerization. [99]

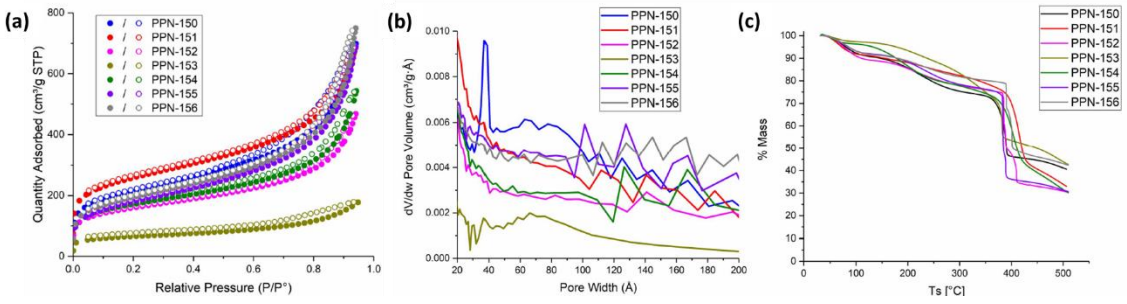

Figure 25a. N_2 absorption isotherms, **b.** BJH pore size distributions, and **c.** TGA decomposition curves, for the PPN 15X series. [99]

The 6 doped PPNs all show a mix of both micro and mesoporosity, with a broad range of fairly large micropores, around 1.2–1.5 nm (Figure 25a, b). The surface areas are typically consistent with that of the undoped PPN-150, except for PPN-153. The phosphonitrilic chloride trimer dopant partially collapses the porous structure. This was most likely due to the reactivity of the labile P-Cl bonds interfering with the desired polymer synthesis. The surface areas of all the doped materials except PPN-151 were lower than that of the undoped material. As the doping occurs during the polymer synthesis as opposed to post-synthetic modification, the loss in surface area was likely due to the increased mass of material added to the synthesis. However, among the doped samples, there appears to be a general trend of improved surface areas and total uptakes for the materials upon incorporation of acidic functionalities in the dopants. Cyanuric acid, an acidic functionality, had the highest surface area of all the PPNs. The phloroglucinol (slightly acidic) doped PPN and ethylene glycol (hydroxyl containing) doped PPN had the second and third highest surface areas, respectively. The trisodium trimetaphosphimate (charged species) doped sample had a surface area comparable to that of the ethylene glycol doped PPN. The hexamethylenetetramine (basic) doped PPN showed the lowest surface area of the nonreactive dopants. Condensation reactions, such as the one used to form PPN-150 can be catalyzed by acidic conditions.[71] This suggests that one of the main effects the dopants may have on the porosity of the sample is through catalyzing or impeding the condensation reaction.

TGA decomposition analysis of the seven PPN samples shows that final decomposition for each material typically occurs around 350–375 °C (Figure 25c). PPN-151 appears to have the highest decomposition temperature, around 390 °C. This high decomposition temperature can be attributed to the stabilizing effects of the cyanuric acid–melamine interaction. This interaction is known to generate a highly stable melamine-cyanurate hydrogen bonding network.[72] Melamine-cyanurate has a significantly improved thermal stability compared to both melamine and cyanuric acid, decomposing at 400 °C, as opposed to the 300 °C decomposition temperature of isolated melamine or cyanuric acid (Figure 24a). It should also be noted that the same TGA curve type cannot be generated by physically mixing PPN-150 with melamine cyanurate or cyanuric acid, suggesting that this change in decomposition behavior is due to a new material phase generated during the polymerization reaction in the presence of cyanuric acid (Figure 27b).

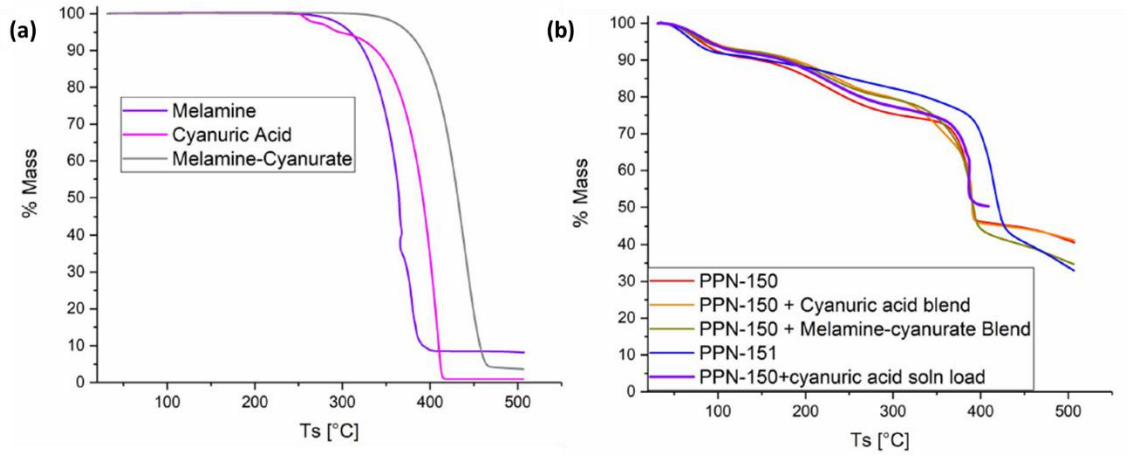

Figure 26. TGA decomposition curves of **a.** Melamine-Cyanurate and its components, **b.** PPN-150 blended with melamine-cyanurate components against PPN-151. [99]

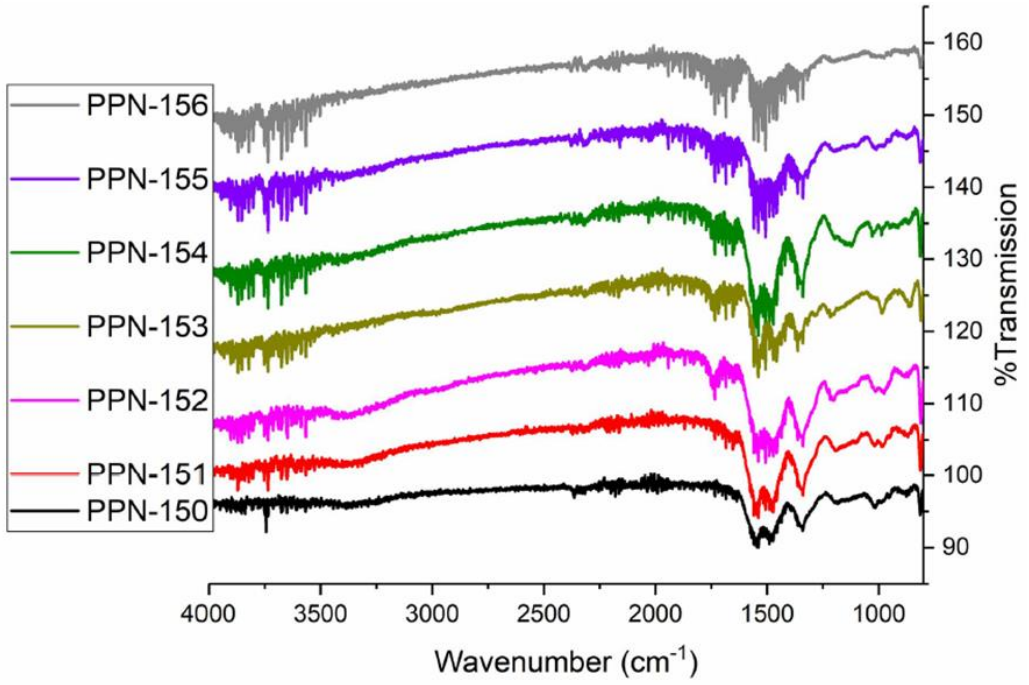

Figure 27. IR Spectra of PPN-15X series of polymers. [99]

IR spectroscopy was performed on the PPN series (Figure 28). Each of the PPN samples showed no noticeable difference from the baseline PPN-150. In order to probe whether the dopant molecules could be observed in the material, higher loadings of the dopants in

the PPN samples were tested: a 50 mol% cyanuric acid was reacted for 1, 2, and 3 d. Only the 1 d reaction appeared to show any presence of cyanuric acid in the IR spectrum of the resulting processed PPN (Figure 29a). However, all three samples showed broadly similar porosities (Figure 29b).

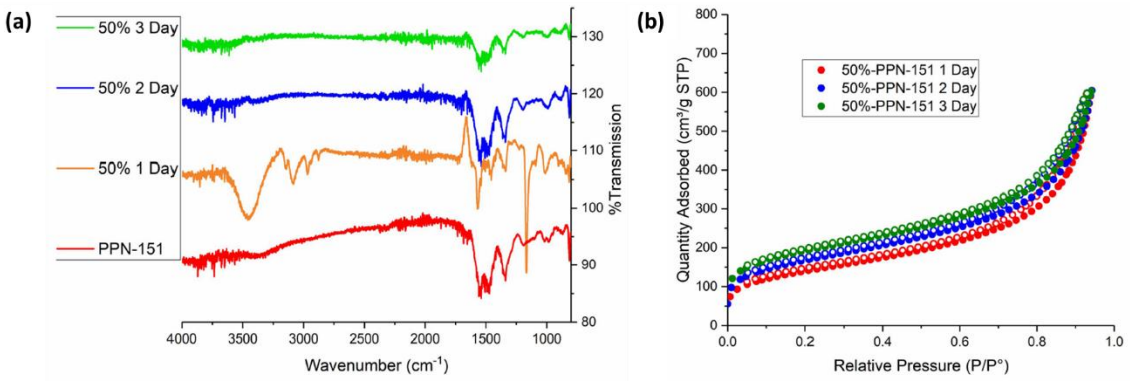

Figure 28a. IR spectra, and **b.** N2 adsorption isotherms, of 50 mol% cyanuric acid PPN-151 at different reaction times. [99]

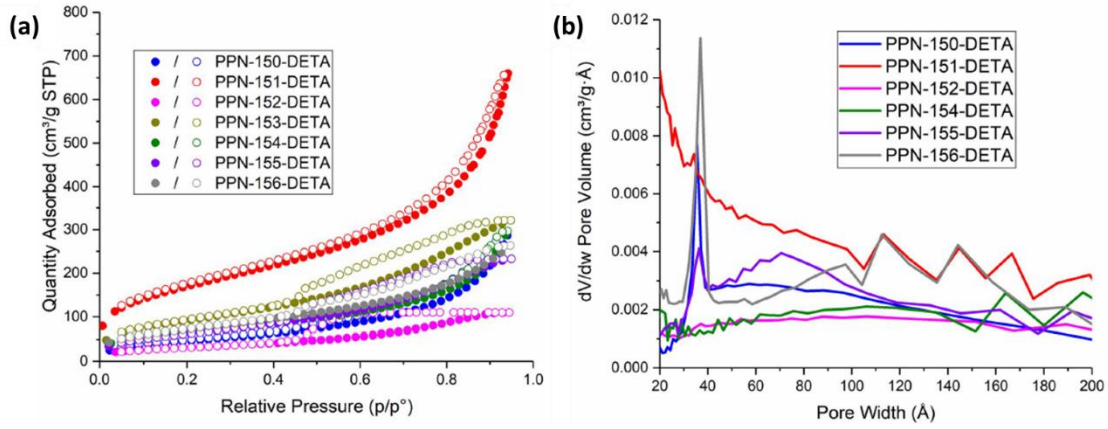

Figure 29a. N2 isotherms of DETA loaded PPN series, **b.** BJH pore size distribution of DETA loaded PPN series. [99]

Upon loading the doped PPNs with DETA, there was a marked drop in surface area, as the loaded amine pooled within the pores of the framework, limiting surface access to the N_2 during gas adsorption measurements (Figure 30). However, there was significant

variation in the surface area drop among the different PPNs. Some PPNs (150, 152, 153) showed a drop in surface area upwards of 50%, while others show an approximate 50% drop (151, 154, 155, 156) (Figure 31a). The PPNs with dopants that showed higher uptakes typically had dopants that contained hydrogen bond donors or acceptors as functional groups (OH, ONa). The PPNs with dopants that showed lower uptakes mainly appeared in systems that had less donating functionalities (tertiary amines, P-Cl bonds). IR spectroscopy of the DETA loaded samples did not show any significant differences between each sample (Figure 31b).

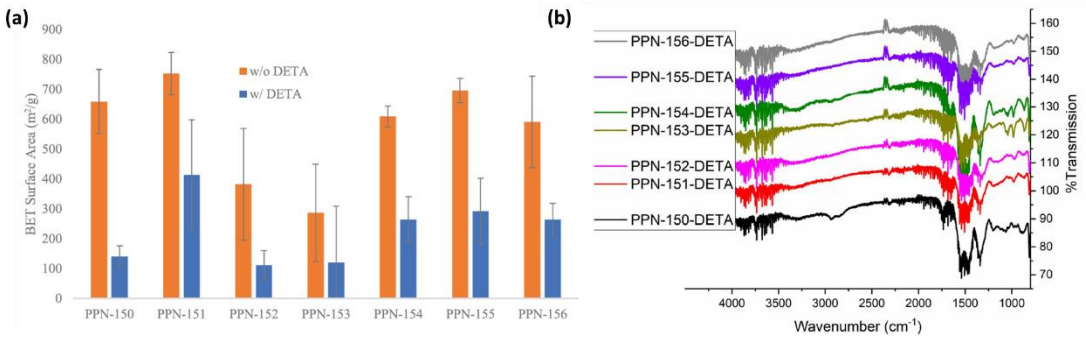

Figure 30a. BET surface area of PPN series with and without DETA loading, **b.** IR spectra of DETA loaded PPN. [99]

From these results, it was hypothesized that the samples with higher surface areas after DETA loading would be better CO_2 capture materials, due to the higher availability of physisorption surfaces. In addition, there was interest in determining the effects of dopant inclusion on the cycling performance, namely, the loss in uptake between subsequent CO_2 adsorption runs.

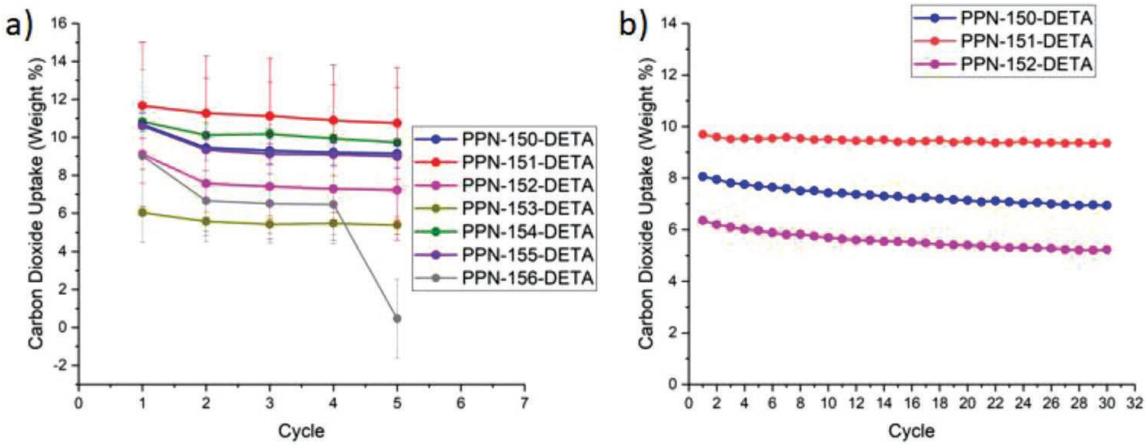

Figure 31a. Five cycle TGA run data using a 15% CO2, 85% N2 gas mixture for PPN-150 series polymers, **b.** Comparison of the top 3 performing sorbents, PPN-150, 151 and 152. [99]

The doped PPNs were investigated via a five-cycle TGA experiment utilizing a 10 min thermal activation at 85 °C between individual cycles, while adsorption was conducted at 40 °C for 40 min using a 15% CO_2:85% N_2 gas mixture (Figure 32a). In general, there was a high degree of variation between synthesized batches, resulting in large standard deviations. Of the six doped materials, four of them showed lower CO_2 uptakes than the undoped PPN-150-DETA, with only PPN-151-DETA and PPN-154-DETA showing higher average uptakes over five cycles. Generally, the initial cycle of loading experiments demonstrated a higher uptake than subsequent cycles. For example, PPN-156-DETA gave an average cycle 1 uptake of 9.02%, whereas the average for cycle 2 was 6.66%. For this material, cycles 3 and 4 showed only a minor loss in uptake performance as compared to cycle 2. The loss of uptake from cycle 1 to cycle 2 was attributed to the incomplete regeneration of the sample after CO_2 adsorption, not the desorption of DETA. This was corroborated by an increase in sample mass after cycle 1, implying that it was unlikely

that material was being lost as a result of the heat cycling. In one iteration of PPN-156-DETA, the baseline mass started at 14.99 mg. After cycle 1, the baseline mass increased to 15.69 mg, which was an increase of 4.7% (Figure 33).

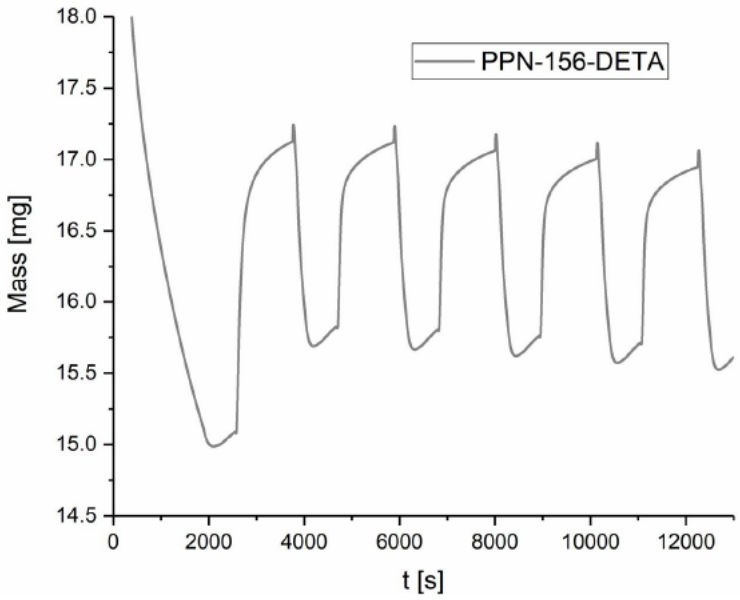

Figure 32. 5 cycle experiment with 85 °C for PPN-156-DETA.[99]

Due to the low loss of cycling performance and high total uptake, further investigation of the long-term cycling of PPN-151-DETA was conducted via extension of the experiment to 30 cycles. For comparison, PPN-150-DETA and PPN-152-DETA were also tested for long-term stability, due to PPN-150-DETA being the baseline material and PPN-152-DETA being a typical material that did not show marked improvement during short-term cycling tests (Figure 32b). Long-term cycling of PPN-150-DETA as well as PPN-152-DETA show a consistent loss in uptake with the progression of the cycles. The loss in performance averaged 14 and 18%, respectively, for PPN-150-DETA and PPN-152-DETA. Additionally, PPN-152-DETA showed an overall lower level of CO_2 uptake as

compared to the undoped PPN-150-DETA. This was likely a result of the lowered surface area and porosity of PPN-152 in comparison with the base material.

The average uptake of PPN-151-DETA remained high relative to the other samples, averaging 9.46%. In addition, the material showed remarkably improved cycling performance over the baseline PPN, only losing 3.6% of its total performance over 30 cycles. This improved cycling performance, in conjunction with the DETA loaded surface areas, suggests that in PPN-151-DETA, CO_2 engages in a slightly different sorption interaction as compared to the other PPNs. This was corroborated by the variable temperature single-component CO_2 isotherms and the calculated heat of adsorption values for PPN-151-DETA which are ≈10 kJ mol^{-1} higher than that of PPN-150-DETA at similar CO_2 loadings (Figure 33).

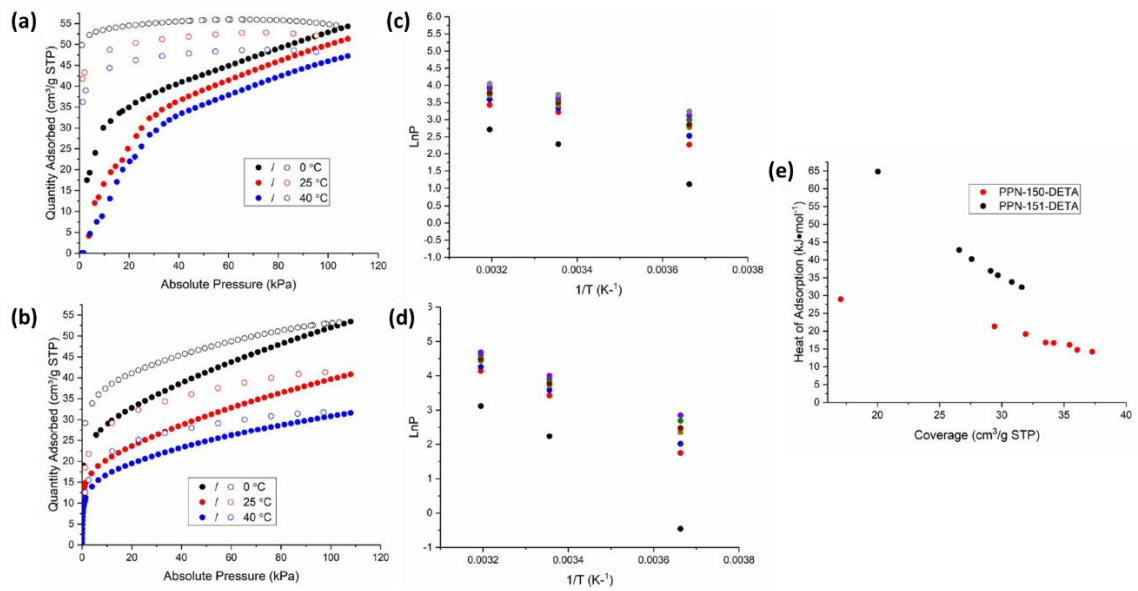

Figure 33. CO_2 isotherms for **a.** PPN-150-DETA, **b.** PPN-151-DETA, Clausius-Clapeyron relationship data for **c.** PPN-150-DETA, **d.** PPN-151-DETA, and **e.** Heat of Adsorption as a function of coverage.[99]

As another method of probing the effect of cyanuric acid on the nature of CO_2 adsorption in PPN-151-DETA, in situ IR testing during gas loading was performed. The data for PPN-150-DETA showed a mix of physisorptively (peak at 2334 cm^{-1}) and chemisorptively (broad shoulder at 1700 cm^{-1}) bound CO_2 in the form of carbamate (Figure 32a). In contrast, the PPN-151-DETA results showed the dominant form of CO_2 in the sample was chemisorptively bound CO_2 (Figure 35b). These results demonstrate that PPN-151-DETA may have a more efficient binding process for CO_2. This was correlated to the heat of adsorption data showing a much stronger initial binding of CO_2 to PPN-151-DETA as compared to PPN-150-DETA.

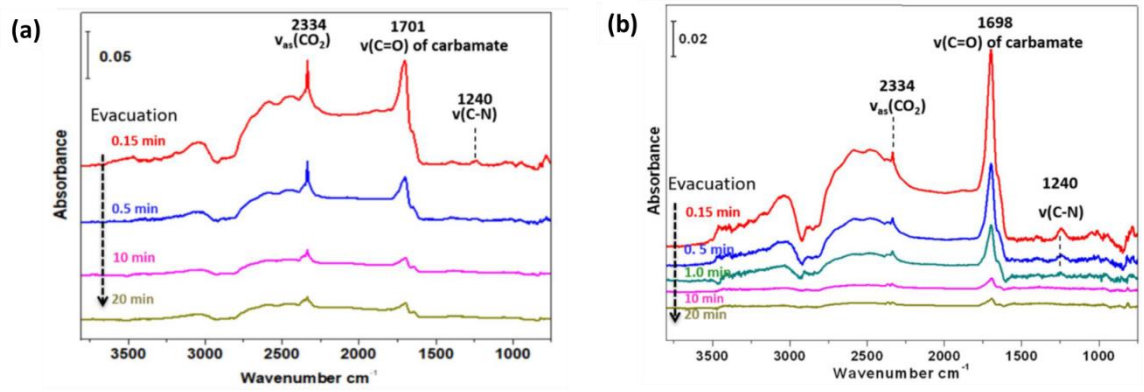

Figure 34. IR spectra of adsorbed CO_2 in **a.** PPN-150-DETA and, **b.** PPN-151-DETA after loading CO_2 at 150 Torr and 40 ºC for ~5 min and subsequent evacuation of gas phase CO_2. [99]

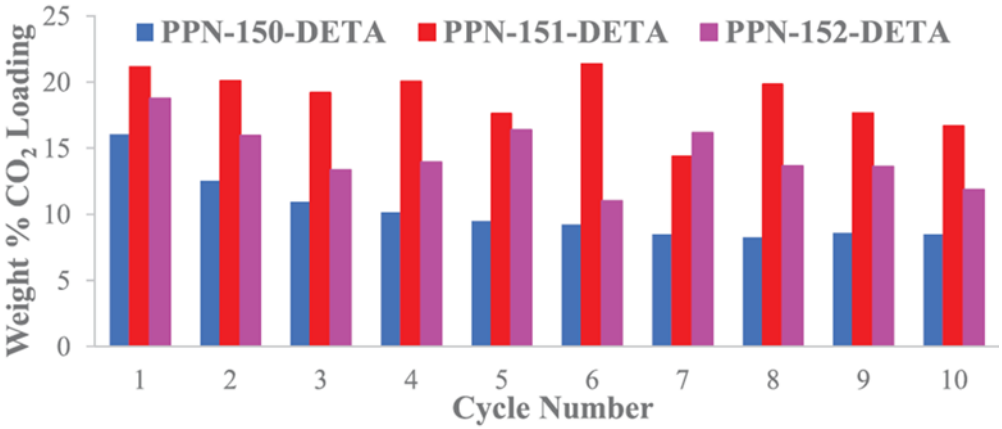

Figure 35. Breakthrough experiment for PPN-150-DETA, PPN-151-DETA, and PPN-152-DETA using a 15% CO_2, 2% H_2O, and 83% N_2 gas mixture. Tests were performed using a 5 mL column containing ≈1 g of loosely packed material. [99]

As PPN-151-DETA was the most promising material, larger scale fixed-bed adsorption testing was conducted using a Quantachrome DynaSorb BT in a breakthrough experiment.[73] In addition, PPN-150-DETA and PPN-152-DETA were also studied to determine if there were any changes in adsorption behavior between TGA and breakthrough analysis (Figure 36). Additionally, the DynaSorb BT allowed for investigations of the cycling behavior under wet gas conditions. In this study, simulated flue gas containing 15% CO_2, 2% H_2O, and 83% N_2 was used to conduct these tests. During breakthrough testing, the sample was placed in an adsorber column and the gas mixture was allowed to flow through the material. This flow through setup allowed for a more efficient and accurate adsorption and desorption as compared to the TGA cycling flow over setup. In the breakthrough experiment, a greater surface area of the material was available for both the adsorption gas stream and the regeneration gas stream.

Overall, the CO_2 uptake of the three samples increases under humid conditions compared to the dry gas adsorption tests. It is believed this occurred due to the improvements in the stoichiometry, where the amine:CO_2 ratio changes from 2:1 to 1:1, in the presence of moisture.[74] However, while this change in the material binding stoichiometry would suggest that the material's uptake capacity should double, this does not take into account the actual working conditions of the breakthrough and TGA experiments. Specifically, they both operate under kinetically controlled, non-equilibrium conditions. As such, the material's real uptake capacity is limited by the ability of CO_2 to diffuse through the material. In particular, the presence of pools of DETA, a viscous liquid, could prevent CO_2 diffusion through the pores located deep within the material. As mentioned before, the BET surface area of the loaded PPNs tends to be significantly lowered compared to the unloaded PPNs. This reduction in surface area is likely the result of the DETA creating pools within the pores of the material. Under the N_2 sorption surface area measurement conditions (77 K), these pools create a solid layer of DETA, blocking N_2 access to the entirety of the internal surface area. Even under working conditions, 40 °C, the viscosity of these DETA pools is likely preventing CO_2 access under simple kinetic gas flow conditions.

PPN-151-DETA showed a massive improvement in performance under wet gas cycling conditions, achieving >20%wt CO_2 as compared to 9.46%wt under dry conditions. Under ideal conditions, the maximum achievable improvement in cycling performance should be 2×. The fact that the experiment resulted in a >2× increase was indicative of either

some improvement in the material efficiency going from TGA to breakthrough experimentation or an improvement in the number of available CO_2 binding sites. One possibility is that some portion of the DETA molecules cannot engage in CO_2 capture under dry conditions as they lack a second equivalent of DETA to act as a proton acceptor. This is corroborated by the heat of adsorption values for PPN-151-DETA, which were calculated from the pure CO_2 isotherms. There was a 22 kJ mol^{-1} (33.9%) reduction in heat of adsorption, going from 64.8 kJ mol^{-1} at 20 cm^3 g^{-1} to 42.8 kJ mol^{-1} at 26.6 cm^3 g^{-1}, which would suggest that there is a significantly lowered affinity toward CO_2 once the initial gas loading has occurred (Figure 33e). For comparison, PPN-150-DETA at a broader range of coverage, 17.0–29.4 cm^3 g^{-1}, only saw a reduction in heat of adsorption of 7.6 kJ mol^{-1}. However, the overall heats of adsorption for PPN-150-DETA are significantly lower, 28.9 and 21.3 kJ mol^{-1}, respectively, which corresponds to a 26.3% reduction in heat of adsorption.

Breakthrough testing of PPN-150-DETA still shows a consistent loss in uptake capacity over many cycles. This was especially noticeable during the first six cycles, where PPN-150-DETA decreases from a 16.0%wt uptake to a 9.2%wt uptake. For comparisons, PPN-151-DETA showed an uptake capacity of 21%wt at both cycle 1 and cycle 6. PPN-152-DETA had a highly variable uptake, going from 18.8%wt in cycle 1 down to 11.0%wt in cycle 6. Part of the issue with PPN-152-DETA was that the slow decomposition of hexamethylenetetramine (HMTA) under aqueous conditions resulted in a release of

ammonia. The free ammonia could both act as an additional CO_2 chemisorptive species, and cause false positive results for CO_2 binding in the DyanSorb BT Instrument TCD.

3.4 Scale Up of Viable Sorbent: PPN-151-DETA

In order to establish the industrial feasibility of PPN-151-DETA, we attempted to produce the material beyond the bench scale. In order to prevent precipitation of melamine cyanurate before the initial polymer gel formation, the cyanuric acid-DMSO solution had to be heated to the reaction temperature (150 °C for the bench scale tests) and was added after the paraformaldehyde had dissolved. Failure to properly heat the cyanuric acid solution or ensure complete dissolution of the paraformaldehyde resulted in a loss of porosity in the final PPN. It should be noted that the larger scale syntheses generally required longer reaction times. For a reaction batch at the 250 g scale, the highest PPN performance was produced after 6 d of reaction time (Figure 37). These results demonstrate that PPN-151-DETA can be utilized as a cost-efficient alternative for industrial post-combustion CO_2 capture.

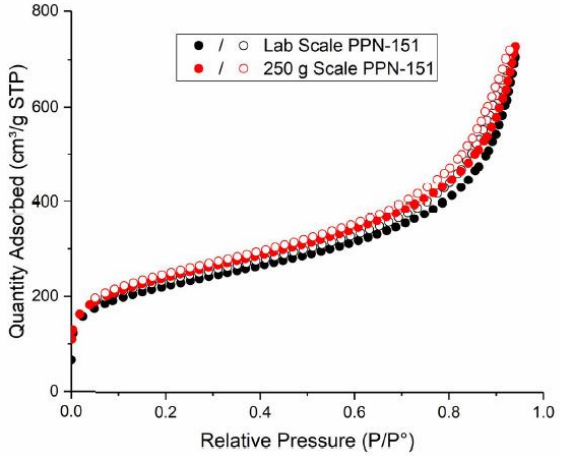

Figure 36. N2 isotherms of Lab scale vs. 250g scale, with surface areas of 853 and 798 cm^3/g respectively. [99]

3.5 Conclusion

Reported herein is a formulation for a family of post-combustion CO_2 capture materials, the PPN-150-DETA family. Each member of the PPN-150-DETA family is differentiated by the incorporation of a different dopant molecule within the PPN during the polymerization reaction. One dopant in particular, cyanuric acid (PPN-151), demonstrated remarkable improvements in performance for PPN-151 as compared to the baseline PPN-150. The improvements for PPN-151 were a higher CO_2 heat of adsorption, improved cyclability, improved performance under wet gas conditions, and improved thermal stability. The post-synthetic amine incorporated polymer, PPN-151-DETA, proved to be a promising commercially viable sorbent for post-combustion CO_2 capture.

3.6 Experimental

All chemicals used in this study were used as received without future purification. The breakthrough measurements were performed on a Quantachrome Breakthrough Instrument with activation temperature of 85 °C and deadtime of 7.3 seconds. The TGA measurements were performed on a Mettler-Toledo TGA/DSC 1. All N_2 adsorption measurements were performed on a Micromeritics BET 2420 instrument at 77K. Variable Temperature CO_2 adsorption isotherms were performed on a Micromeritics BET 2020 instrument using an ice water bath (for 0 °C) or a Micromeritics Iso Controller (25 °C and 40 °C). Heat of Adsorption values were collected using the Clausius-Capeyron equation and CO_2 adsorption data collected at 0 °C, 25 °C, and 40 °C.

FTIR data was collected using a Shimadzu IRAffinity-1. SEM images were collected using a JEOL-JSM-7500F. Density measurements for both skeletal and bulk PPN-150-DETA were performed by Micromeretics Analytical Services. The in-situ IR spectroscopic data were obtained using a Nicolet 6700 Fourier transform IR spectrometer (Thermo Scientific Inc, US) equipped with a liquid N2-cooled mercury cadmium telluride MCT-A detector. A pressure cell (SpecacLtd, UK-product number P/N 5850c) was placed in the sample compartment of the IR spectrometer with the sample at the focal point of the beam. Elemental Analysis was performed by Atlantic Microlabs.

3.6.1 Laboratory Scale PPN-150

4 mL of DMSO was added to a 20 mL vial and heated to 120 °C, to this was added melamine (377 mg, 2.99 mmol), which was allowed to fully dissolve. Paraformaldehyde (202 mg, 6.73 mmol, 2.25 eq) was then added as a powder to the vial. The paraformaldehyde was allowed to dissolve and the vial was sealed and placed in an oven at 150 °C or 170 °C for 3 days. The vial was then removed from the oven and allowed to cool to room temperature. The resulting monolith was then ground up via mortar and pestel and the powder washed three times with 5 mL of acetone, three times with 5 mL of tetrahydrofuran, three times with 5 mL of dichloromethane, and three times with 5 mL of methanol. The solid was then dried under vacuum at 120 °C overnight, yielding 440 mg of a white solid.

3.6.2 Alkylamine loading procedure

100 mg of PPN-150 series polymer was loaded into a 4 mL vial. To this was added 1.5 mL of a solvent (cyclohexane or hexane) and 300 μL of DETA. The vial was then placed in a sonicator bath set at 55 °C for 3 hours. Upon completion, the solid was filtered, washed with tetrahydrofuran, and dried at 85 °C for 30 min to give 100 mg of white solid.

3.6.3 250 g PPN-151 Synthesis

1.88 L of DMSO was heated to 120 °C in a 3 L beaker while at the same time a 10 L jacketed glass reactor connected to a circulating oil heater is heated to 120 °C. Once the beaker of DMSO has reached 120 °C melamine (201.6 g 1.598 mol) was added slowly and allowed to completely dissolve. The melamine solution was then added to the reactor and the reactor was heated up to 150 °C. 200 mL of DMSO is heated to 120°C in a 500 mL beaker, to this was added cyanuric acid (15.5 g, 0.120 mol, 0.075 eq). Once the reactor reached 150 °C, paraformaldehyde (108.0 g, 3.596 mol, 2.25 eq) was added as a fine powder and allowed to dissolve completely in the DMSO/melamine solution. To this was added the DMSO/cyanuric acid solution. The reactor was sealed and wrapped in insulation and allowed to sit at 150 °C for 6 days. Upon cooling to room temperature, the solid monolith was removed from the reactor, ground up in a mortar and pestel, and washed three times with 1.3 L of acetone, three times with 1.3 L of tetrahydrofuran, three times with 1.3 L of dichloromethane, and three times with 1.3 L of methanol. The solid was then placed in a sealed reactor with a suspended stirrer and allowed to soak in methanol at 60 °C for 24 hours before filtration. This solvent exchange was conducted twice. The solid was then allowed to air dry in a hood

overnight before being placed in a vacuum oven 120 °C for two days, producing 275 g of white solid.

CHAPTER IV

APPLICATIONS OF COMPOSITE MATERIALS

4.1 Metal-Organic Frameworks – Potential Applications

While there exists a wealth of information in the literature concerning metal-organic frameworks (MOFs), it is rare to see them being employed in industrial or commercial processes. Although no longer in its infancy, MOF chemistry still has many hidden depths that have yet to be discovered. One of the biggest challenges faced by MOF chemists is the scale of MOF synthesis. At present, there are few MOFs that can be synthesized at a large enough scale, that are also economically feasible. Many MOF syntheses produce these materials at a milligram scale and cannot be effectively scaled to produce materials on the gram or kilogram scale. While there are over hundreds of existing MOF variations, a key player in chemical sales, Millipore-Sigma, only lists 5 variations of MOFs,[75] commercially listed as Basolites®, that are available for purchase. In addition to that, there are other specialized companies that fill the niche of providing commercial MOFs. Additionally, many MOFs do not retain structural stability outside of solution, with the solvent evacuation causing pore collapse, and the subsequent loss in porosity. It is of interest to develop methods to utilize MOFs in the solid state, while maintaining their functionality, without the reliance on solvent. As such, this chapter will discuss the synthesis of MOF-composite materials, focusing primarily on MOFs that are commercially available.

4.2 Polymer-MOF Composites for Flame Retardancy

Flame retardants are materials that are produced during combustion, that help to reduce the spread of flames, should the object catch fire. Early flame retardants, such as polychlorinated biphenyls (PCBs), while effective at the time, proved to have toxic side effects on humans.[76–78] Since then, we have seen a rise in demand for alternative flame retardants. While brominated flame retardants initially replaced PCBs, these were also found to have significant side effects,[79–82] either from the gradual release of the compound into the surrounding areas, or release of the compounds when the materials are subject to higher temperatures or flames, and are slowly being phased out. The current frontrunners for alternative flame retardants are organophosphates,[83,84] and polymeric materials,[85,86] which have been targeted as a replacement for existing brominated flame retardants. However, an area that might have been overlooked is the use of certain transition metals in flame retardants.[87] There have been a few literature works that have combined MOFs with polymers for enhanced flame retardance, that have focused on introducing phosphorous species into the MOF ligand, in order to take advantage of the flame retardant properties of the organophosphate compounds.[88,89] In this study, we will investigate the effect of various functional groups within MOFs that have previously demonstrated flame retardant properties, to determine the effect they have on the combustion of polymeric materials.

4.3 Initial MOF Selection

Preliminary testing was conducted with 2 species of MOF, UiO-66,[30,90,91] and PCN-250,[23] which can both be reliably produced at the gram scales needed for polymer impregnation for cone calorimetry testing. In collaboration with Dr. Wang's lab in the Department of Chemical Engineering at Texas A&M University, hypothesized that the inclusion of MOFs into established polymers, such as polymethylmethacrylate (PMMA), would allow for the incorporation of desired functionality into the polymer for flame retardancy, without the need for modification of the polymeric backbone, eliminating the time that would have been required to develop and optimize a new monomer and polymer synthesis. Additionally, MOFs can consistently be synthesized at the nano scale, and failing that, can be mechanically reduced to smaller particles for ease of suspension in the polymer matrix, without having to worry about phase separation.

While the tested materials, UiO-66 and PCN-250, do not possess all the ideal qualities for flame retardancy, both species can be used in the dispersion testing for MOF in PMMA while testing the efficacy of their inherent flame retardant effects.

UiO-66 is a zirconium based MOF, with a 12 coordinated Zr_6 cluster and benzene dicarboxylate (BDC) organic linker. The $Zr_6O_4(OH)_4$ nodes possess six Zr^{4+} ions in octahedral geometry and four oxygen atoms or hydroxyls at the centers of each of the octahedral faces, forming a fcu topology. UiO-66 is well known for its good thermal stability and ability to withstand a variety of solvents with minimal degradation. This is ideal for our purpose as polymer processing often requires high temperatures for curing and often is dependent on a specific solvent. The stability of UiO-66 means that it can be

incorporated in a variety of polymers without significant physical or chemical changes. Additionally, zirconium has a demonstrated ability to enhance the formation of a char layer in polymers upon combustion through polymer dehydrogenation. Given this information, it was determined that UiO-66 was a good candidate for initial testing of the polymer-MOF composites.

PCN-250, also known as MIL-127, is a framework comprised of a trimeric metal cluster, formed by three Fe(III) octahedra sharing a central μ3-oxo, which is then linked by 6 ABTC ligands (ABTC = 3, 3‘, 5, 5‘-azobenzenetetracarboxylate) to form a soc net. Upon heating at high temperatures, the ABTC ligand decomposes, liberating N_2,[92] an inert gas, which can aid in the muffling of flames, by reducing the oxygen availability at the combustion site. Additionally, previous collaboration with *framergy*™ resulted in the development of a procedure for bulk generation of PCN-250, allowing us to easily obtain the amounts needed for testing.

4.4 Results and Analysis

In this study, we investigated the effect that incorporation of MOFs had on the flame retardance on a polymer, PMMA. PMMA is a transparent and rigid thermoplastic material widely used as a shatterproof replacement for glass. PMMA is often used as a model fuel in flame tests as the combustion is clean and does not produce char layer. Its thermal decomposition mechanism has been well documented in the literature and it reliably decomposes in the temperature range of 315-400°C.[93–95]

Previous work by our collaborators, Wang et. Al. also utilized PMMA as a medium for testing the flame retardant capabilities of a PMMA-silica nanocomposites.[96] Results of this study, that tested the doping of PMMA with 1-4% silica, indicated that the composite demonstrated a lower ignition temperature, a phenomenon commonly seen in polymer nanocomposites. Although the ignition temperature was lowered, it is not a key factor in determining the flame retardancy. Using the heat release rate, total heat release and the mass loss rate, it was determined that the inclusion of silica in the PMMA samples improved the flame retardancy performance, with non-crosslinked samples performing slightly better, and the flame retardancy increasing with the mass% of silica in the sample. This was a result of the formation of a nanosilica-rich layer upon combustion, which forms a protective outer layer, preventing further thermal degradation of the polymer. While effective, this method does result in lowered ignition temperature and increased soot formation, which can lead to other negative effects.

In this study, samples of PMMA (100mm x 100mm x 5mm) were prepared and subjected to cone calorimeter analysis. A series of UiO-66/PMMA samples were produced, 0.5, 1.0 and 1.5 wt% UiO-66 respectively, with a sample of neat PMMA as a control. Samples were tested under an irradiance heat flux of 50kW m^{-2} in order to simulate the conditions of a developing fire (to the standard of ASTM E 1354).[97]

One of the factors studied in this experiment is the heat release rate, a critical fire response property. The heat release rate of a compound is the primary driving force of fire spread and is a determining factor of other reactions, such as the production of CO, CO_2 and the

rate of decomposition. Of this, the peak heat release rate is of significance as it is an indicator of the maximum flame temperature and the rate of flame spreading.

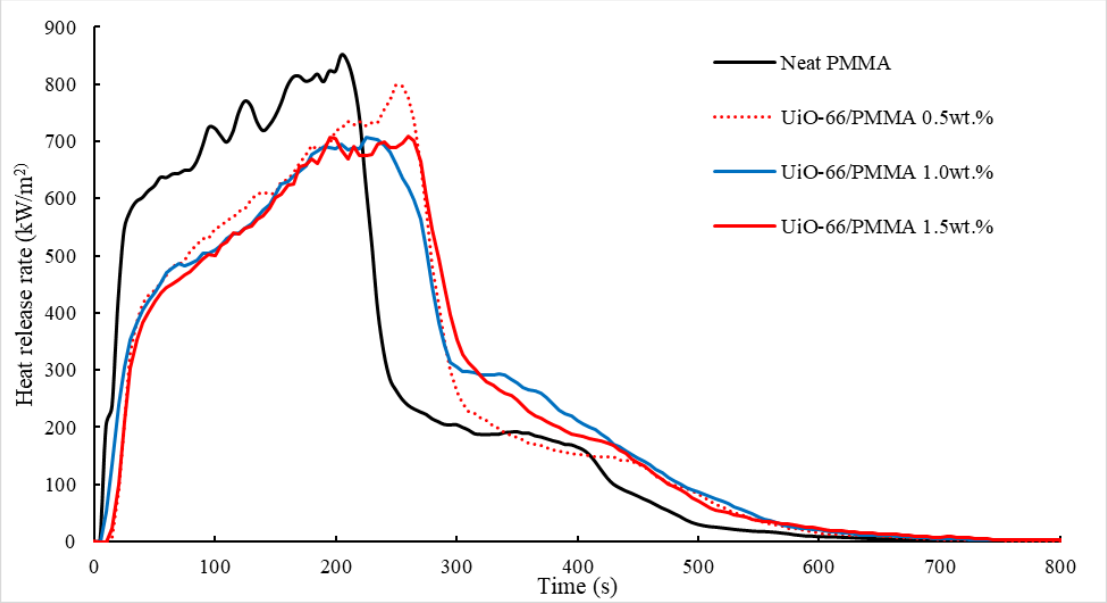

Figure 37. Heat release rate profiles of the UiO-66/PMMA composites

The heat release rate profiles for the 4 samples (Figure 38) indicate a change in heat release profile of the PMMA upon addition of UiO-66. From the graph, we note the increase in time to ignition with an increase in UiO-66 loading. In contrast with the previous studies with silica, where the introduction of additives lowered the ignition temperature, the MOF-polymer composite has a longer time before ignition, indicating a better resistance to combustion. As previously mentioned, the flame retardation of a material is not directly dependent on the ignition, but the maximum heat release rate and flame spread. In this case, we note that the composites have a lower heat profile than neat PMMA, and a lower maximum heat release rate, with a drop in the maximum from 0.5% to 1.0%, with the

1.5% sample having a similar release profile to the 1.0% sample. This decrease in peak heat release indicates that the composites have a lower combustion intensity than the neat polymer. Thus, we can conclude that the addition of UiO-66 to PMMA results in an increase in flame retardant properties.

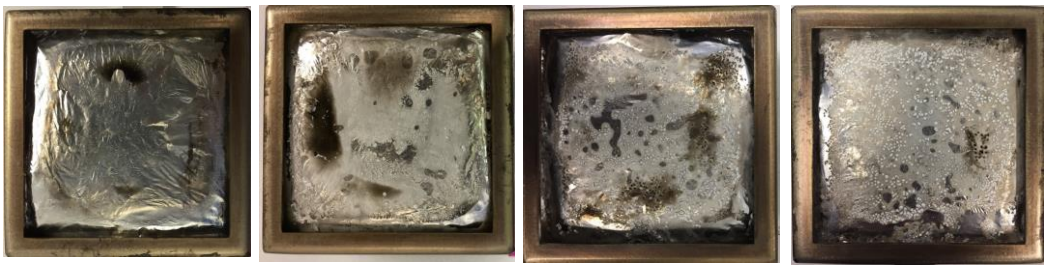

Figure 38. Combustion residues after cone calorimeter tests under an irradiance heat flux of 50 kW/m2 of **a.** neat PMMA, **b.** UiO-66/PMMA 0.5 wt.%, **c.** UiO-66/PMMA 1.0 wt.%, and **d.** UiO-66/PMMA 1.5 wt.%.

In addition to studying the heat release profiles, we also observe the visual effect of combustion testing on the material. In the control, neat PMMA (Figure 39a), the combustion test results in a relatively clean looking sample, with little to no combustion residue. For the composite samples, a layer of white solids remains after combustion. This layer was formed during combustion, accumulating on the PMMA surface, reducing the heat transfer to the bulk polymer beneath, suppressing the release of solid fuel for combustion. Additionally, a black char layer was also observed for these samples, which also aids in flame retardation, as it forms another protective layer.

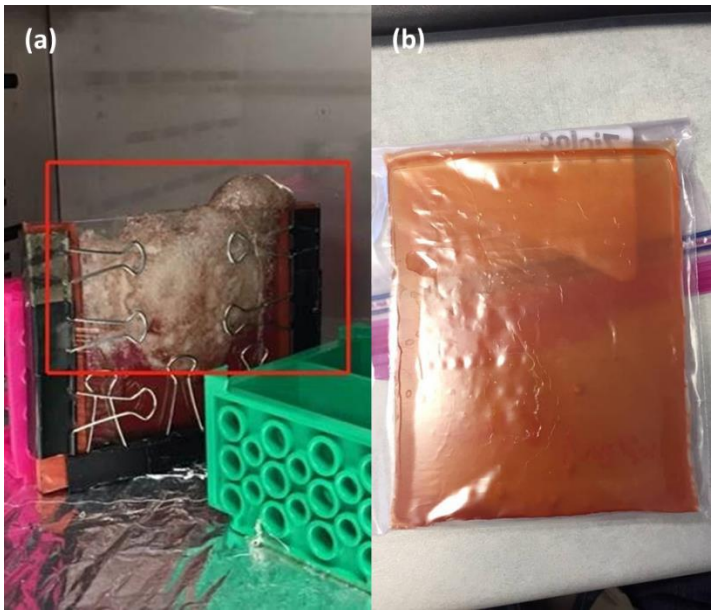

Figure 39a. Unsuccessful, and **b.** successful attempts to produce a PMMA/PCN-250 composite under the same conditions

Attempts at forming a MOF composite using the PMMA and PCN-250 were inconsistent when employing the same reaction conditions. Further optimization of this process must be conducted.

4.4 Methodology

4.4.1. Synthesis of UiO-66

UiO-66 was prepared using a modified literature synthesis.[90] BDC (0.6 mmol) and acetic acid (0.36mol) were added to a 250mL round bottom flask containing 140mL DMF at room temperature. The solution was heated to 120 °C in an oil bath and a solution of 10ml DMF and $ZrCl_4$ (0.6 mmol) was added while stirring. The solution was left to react at this temperature for 6 hours without stirring. After the solution was collected, the product was

subjected to 3 washes with DMF, followed by 3 washes with methanol and dried in a 60 °C oven.

4.4.2 Synthesis of PCN-250

PCN-250 was obtained from framergy™, using the synthesis reported by Feng *et al*.[23]

4.4.3 Synthesis of PMMA composites

PMMA composites were prepared as reported by Shen *et al*..[96] MMA monomer was placed in a glass reaction vial sealed with a silicone septum. MOF particles were added to the monomer under magnetic stirring at various loadings (0.5, 1.0 and 1.5 mass%). Reaction was left to stir for 30 minutes, followed by sonication for 30 minutes, which allowed for the degasification of dissolved oxygen. The initiator, 1,1′-Azobis(cyclohexanecarbonitrile) (ABCN), was added to the mixture at 0.2 mass% with respect to MMA. Nitrogen gas was bubbled through the solution for 10 minutes under continuous stirring. The polymer-MOF mixture was poured into a glass mold, which was then clamped together and placed in a large oil bath for 24 hours at 70 °C. Upon completion of the curing process, the composite was released from the mold and cut to 100mm x 100mm x 5mm in preparation for cone calorimetry testing.

4.4.4. Cone Calorimeter Testing

All samples were tested according to ASTM E 1354 using a cone calorimeter from Fire Testing Technology Limited (FTT). Samples were directly exposed to a heater with the heat flux of 50 kW m^{-2} and evaluated in the horizontal orientation. The unexposed surfaces of these samples were wrapped in aluminum foil prior to testing. The samples were placed in retainer frame with a thin wire cross on the exposed surface to prevent bucking before

burning. The ambient temperature was in a range of 20.2 to 20.9 °C, ambient pressure in the range of 97.994 to 98.148 kPa, and the relative humidity was in the range of 27–28%.

CHAPTER V

CONCLUSIONS

In this dissertation, we explored the modification of various porous materials for three applications: methane storage, carbon capture, and flame retardants. The research presented above demonstrates the diversity and adaptability of porous materials, focusing on fully utilizing existing, well studied materials and modifying them to suit our needs. With many of these hybrid porous materials, the foray into commercial applications is still in its infancy. While the discovery of novel materials is both exciting and educational, utilizing well studied materials provides the benefit of existing literature, known methods of characterization, as well as a benchmark for the performance of adapted materials, effectively minimizing the time required to take these materials to commercial applications. Given the wealth of existing materials available for our perusal, the possibilities are endless.

5.1 Methane Storage

The aim of this project was to develop a stable, scalable, cost effective material for use in methane capture. Within this project, we discovered a method for inducing mesoporosity in an existing microporous MOF, PCN-250. This method allowed for the simple, post-synthetic treatment of the material, which resulted in a hierarchical structure, with micropores (ca 8 Å) and mesopores (ca 38 Å). This was then combined with existing methods for improving the energy density and uptake of methane, resulting in the development of HAANG, High-Alkane Adsorbed Natural Gas. Comparison of MOF pore

size and alkane van der Waals' radii indicated a size mismatch with the pristine MOF, with improved performance when mesopores were induced in the material. While doping the alkane into the framework resulted in improved methane capacity, it was noted that desorption of the alkane occurred over time, with longer chains experiencing better retention. As a result, alternative molecules that also possessed long chain alkanes were tested with the material, to determine if tethering would improve the recycling performance of the material, with fatty acids proving to have a similar function, with the added benefit of tethering to the metal nodes within the structure. Most importantly, it was determined that the production of the best performing material was scalable, without any major changes to the process.

5.2 Carbon Capture

In this section, we explored a solid sorbent for carbon capture, aiming at developing a low cost material, with low regenerative energy, to provide an alternative to existing state-of-the-art carbon capture from flue gas, monoethanolamine (MEA) solutions. An existing polymer, melamine-formaldehyde, was studied for this purpose. Introduction of a cyanuric acid dopant into the framework resulted in improved carbon dioxide uptake. Analysis of the base polymer, PPN-150, and the modified polymer, PPN-151, indicated that they participated in two mechanisms of carbon dioxide capture, physisorption and chemisorption. Analysis of the materials indicated that while PPN-150 utilized both pathways, PPN-151 experienced minimal physisorption, instead forming a carbamate. While heats of adsorption for chemisorption are often high, with MEA solutions ranging

from 80 -185 kJ mol^{-1}, PPN-151 had a surprisingly low heat of adsorption, from 43 – 65 kJ mol^{-1}, combining the benefits of solid sorbents and chemisorption. Additionally, the material could be synthesized at a 250g scale while retaining a high carbon capture performance. Most importantly, the materials required to synthesize the polymer are low cost, with most of the production costs stemming from the synthesis solvent, DMSO.

5.3 Flame Retardant

The study of flame retardant polymer-MOF composites is in early stages, with much more testing needed to be done. At present, only 2 MOFs have been tested as additives, demonstrating the formation of composites and the varying effect that different MOFs have on the flame retardant performance of the polymer. As such, at low loading levels, incorporation of UiO-66, a zirconium based MOF, has shown to improve the flame retardance of PMMA. Given the wealth of options available for MOF species, there is much more to be explored in this area.

REFERENCES

(1) Wang, X.; Bu, X.; Feng, P. Porous Inorganic Materials. In *Encyclopedia of Inorganic and Bioinorganic Chemistry*; Scott, R. A., Ed.; John Wiley & Sons, Ltd: Chichester, UK, 2011; p eibc0264. https://doi.org/10.1002/9781119951438.eibc0264.

(2) Zones, S. I.; Davis, M. E. Zeolite Materials: Recent Discoveries and Future Prospects. *Curr. Opin. Solid State Mater. Sci.* **1996**, *1* (1), 107–117. https://doi.org/10.1016/S1359-0286(96)80018-0.

(3) Chaikittisilp, W.; Ariga, K.; Yamauchi, Y. A New Family of Carbon Materials: Synthesis of MOF-Derived Nanoporous Carbons and Their Promising Applications. *J Mater Chem A* **2013**, *1* (1), 14–19. https://doi.org/10.1039/C2TA00278G.

(4) Butova, V. V.; Soldatov, M. A.; Guda, A. A.; Lomachenko, K. A.; Lamberti, C. Metal-Organic Frameworks: Structure, Properties, Methods of Synthesis and Characterization. *Russ. Chem. Rev.* **2016**, *85* (3), 280–307. https://doi.org/10.1070/RCR4554.

(5) Janiak, C.; Vieth, J. K. MOFs, MILs and More: Concepts, Properties and Applications for Porous Coordination Networks (PCNs). *New J. Chem.* **2010**, *34* (11), 2366. https://doi.org/10.1039/c0nj00275e.

(6) Ding, S.-Y.; Wang, W. Covalent Organic Frameworks (COFs): From Design to Applications. *Chem Soc Rev* **2013**, *42* (2), 548–568. https://doi.org/10.1039/C2CS35072F.

(7) Wu, D.; Xu, F.; Sun, B.; Fu, R.; He, H.; Matyjaszewski, K. Design and Preparation of Porous Polymers. *Chem. Rev.* **2012**, *112* (7), 3959–4015. https://doi.org/10.1021/cr200440z.

(8) O'Keeffe, M. NEW MICROPOROUS CRYSTALLINE MATERIALS: MOFS, COFS, AND ZIFS. 11.

(9) Barrios, E.; Fox, D.; Li Sip, Y. Y.; Catarata, R.; Calderon, J. E.; Azim, N.; Afrin, S.; Zhang, Z.; Zhai, L. Nanomaterials in Advanced, High-Performance Aerogel Composites: A Review. *Polymers* **2019**, *11* (4), 726. https://doi.org/10.3390/polym11040726.

(10) Ahmed, E. M. Hydrogel: Preparation, Characterization, and Applications: A Review. *J. Adv. Res.* **2015**, *6* (2), 105–121. https://doi.org/10.1016/j.jare.2013.07.006.

(11) Cook, T. R.; Zheng, Y.-R.; Stang, P. J. Metal–Organic Frameworks and Self-Assembled Supramolecular Coordination Complexes: Comparing and Contrasting the Design, Synthesis, and Functionality of Metal–Organic Materials. *Chem. Rev.* **2013**, *113* (1), 734–777. https://doi.org/10.1021/cr3002824.

(12) Sing, K. S. W.; Everett, D. H.; Haul, R. A. W.; Moscou, L.; Pierotti, R. A.; Rouquerol, J.; Siemieniewska, T. Reporting Physisorption Data for Gas/Solid Systems. In *Handbook of Heterogeneous Catalysis*; Ertl, G., Kn��zinger, H., Sch��th, F., Weitkamp, J., Eds.; Wiley-VCH Verlag GmbH & Co. KGaA: Weinheim, Germany, 2008; p hetcat0065. https://doi.org/10.1002/9783527610044.hetcat0065.

(13) Brandt, A. R.; Heath, G. A.; Kort, E. A.; O'Sullivan, F.; Pétron, G.; Jordaan, S. M.; Tans, P.; Wilcox, J.; Gopstein, A. M.; Arent, D.; Wofsy, S.; Brown, N. J.; Bradley,

R.; Stucky, G. D.; Eardley, D.; Harriss, R. Methane Leaks from North American Natural Gas Systems. *Science* **2014**, *343* (6172), 733. https://doi.org/10.1126/science.1247045.

(14) Menon, V. C.; Komarneni, S. Porous Adsorbents for Vehicular Natural Gas Storage: A Review. *J. Porous Mater.* **1998**, *5* (1), 43–58. https://doi.org/10.1023/A:1009673830619.

(15) Makal, T. A.; Li, J.-R.; Lu, W.; Zhou, H.-C. Methane Storage in Advanced Porous Materials. *Chem. Soc. Rev.* **2012**, *41* (23), 7761–7779. https://doi.org/10.1039/C2CS35251F.

(16) Kondo, M.; Yoshitomi, T.; Matsuzaka, H.; Kitagawa, S.; Seki, K. Three-Dimensional Framework with Channeling Cavities for Small Molecules: [M2(4, 4′-Bpy)3(NO3)4]·xH2On (M □ Co, Ni, Zn). *Angew. Chem. Int. Ed. Engl.* **1997**, *36* (16), 1725–1727. https://doi.org/10.1002/anie.199717251.

(17) Fu, J.; Tian, Y.; Wu, J. Seeking Metal–Organic Frameworks for Methane Storage in Natural Gas Vehicles. *Adsorption* **2015**, *21* (6), 499–507. https://doi.org/10.1007/s10450-015-9688-2.

(18) Celzard, A.; Fierro, V. Preparing a Suitable Material Designed for Methane Storage: A Comprehensive Report. *Energy Fuels* **2005**, *19* (2), 573–583. https://doi.org/10.1021/ef040045b.

(19) Düren, T.; Sarkisov, L.; Yaghi, O. M.; Snurr, R. Q. Design of New Materials for Methane Storage. *Langmuir* **2004**, *20* (7), 2683–2689. https://doi.org/10.1021/la0355500.

(20) Ma, S.; Sun, D.; Simmons, J. M.; Collier, C. D.; Yuan, D.; Zhou, H.-C. Metal-Organic Framework from an Anthracene Derivative Containing Nanoscopic Cages Exhibiting High Methane Uptake. *J. Am. Chem. Soc.* **2008**, *130* (3), 1012–1016. https://doi.org/10.1021/ja0771639.

(21) Peng, Y.; Krungleviciute, V.; Eryazici, I.; Hupp, J. T.; Farha, O. K.; Yildirim, T. Methane Storage in Metal–Organic Frameworks: Current Records, Surprise Findings, and Challenges. *J. Am. Chem. Soc.* **2013**, *135* (32), 11887–11894. https://doi.org/10.1021/ja4045289.

(22) Low, J. J.; Benin, A. I.; Jakubczak, P.; Abrahamian, J. F.; Faheem, S. A.; Willis, R. R. Virtual High Throughput Screening Confirmed Experimentally: Porous Coordination Polymer Hydration. *J. Am. Chem. Soc.* **2009**, *131* (43), 15834–15842. https://doi.org/10.1021/ja9061344.

(23) Feng, D.; Wang, K.; Wei, Z.; Chen, Y.-P.; Simon, C. M.; Arvapally, R. K.; Martin, R. L.; Bosch, M.; Liu, T.-F.; Fordham, S.; Yuan, D.; Omary, M. A.; Haranczyk, M.; Smit, B.; Zhou, H.-C. Kinetically Tuned Dimensional Augmentation as a Versatile Synthetic Route towards Robust Metal–Organic Frameworks. *Nat. Commun.* **2014**, *5* (1), 1–9. https://doi.org/10.1038/ncomms6723.

(24) Ikealumba, W. C.; Wu, H. Some Recent Advances in Liquefied Natural Gas (LNG) Production, Spill, Dispersion, and Safety. *Energy Fuels* **2014**, *28* (6), 3556–3586. https://doi.org/10.1021/ef500626u.

(25) Arthur, M. H.; Y. A. Russell, Jr; Nelly, H. M. U. S. Patent. 2,535,148, 1950.

(26) Xia; Ma; Guo; Hua, C. Determination and Study of the Solubility of Methane in Mixtures of Methanol plus Various Hydrocarbons at High Pressures. *J. Chem. Eng. Data* **2006**, *51* (3), 1035–1038. https://doi.org/10.1021/je050517w.

(27) Ornstein, J. M.; Odzemir, O. K. U. S. Patent,. 15,112,921, 2016.

(28) Liu, Y.; Eubank, J. F.; Cairns, A. J.; Eckert, J.; Kravtsov, V. C.; Luebke, R.; Eddaoudi, M. Assembly of Metal–Organic Frameworks (MOFs) Based on Indium-Trimer Building Blocks: A Porous MOF with Soc Topology and High Hydrogen Storage. *Angew. Chem. Int. Ed.* **2007**, *46* (18), 3278–3283. https://doi.org/10.1002/anie.200604306.

(29) Chevreau, H.; Permyakova, A.; Nouar, F.; Fabry, P.; Livage, C.; Ragon, F.; Garcia-Marquez, A.; Devic, T.; Steunou, N.; Serre, C.; Horcajada, P. Synthesis of the Biocompatible and Highly Stable MIL-127(Fe): From Large Scale Synthesis to Particle Size Control. *CrystEngComm* **2016**, *18* (22), 4094–4101. https://doi.org/10.1039/C5CE01864A.

(30) Eddaoudi, M. Systematic Design of Pore Size and Functionality in Isoreticular MOFs and Their Application in Methane Storage. *Science* **2002**, *295* (5554), 469–472. https://doi.org/10.1126/science.1067208.

(31) Jiang, H.-L.; Makal, T. A.; Zhou, H.-C. Interpenetration Control in Metal–Organic Frameworks for Functional Applications. *Coord. Chem. Rev.* **2013**, *257* (15–16), 2232–2249. https://doi.org/10.1016/j.ccr.2013.03.017.

(32) Cai, G.; Jiang, H.-L. A Modulator-Induced Defect-Formation Strategy to Hierarchically Porous Metal-Organic Frameworks with High Stability. *Angew. Chem. Int. Ed Engl.* **2017**, *56* (2), 563–567. https://doi.org/10.1002/anie.201610914.

(33) Kim, Y.; Yang, T.; Yun, G.; Ghasemian, M. B.; Koo, J.; Lee, E.; Cho, S. J.; Kim, K. Hydrolytic Transformation of Microporous Metal–Organic Frameworks to Hierarchical Micro- and Mesoporous MOFs. *Angew. Chem. Int. Ed.* **2015**, *54* (45), 13273–13278. https://doi.org/10.1002/anie.201506391.

(34) Jiang, J.; Furukawa, H.; Zhang, Y.-B.; Yaghi, O. M. High Methane Storage Working Capacity in Metal–Organic Frameworks with Acrylate Links. *J. Am. Chem. Soc.* **2016**, *138* (32), 10244–10251. https://doi.org/10.1021/jacs.6b05261.

(35) Liang, C.-C.; Shi, Z.-L.; He, C.-T.; Tan, J.; Zhou, H.-D.; Zhou, H.-L.; Lee, Y.; Zhang, Y.-B. Engineering of Pore Geometry for Ultrahigh Capacity Methane Storage in Mesoporous Metal–Organic Frameworks. *J. Am. Chem. Soc.* **2017**, *139* (38), 13300–13303. https://doi.org/10.1021/jacs.7b08347.

(36) Karaipekli, A.; Sarı, A. Capric–Myristic Acid/Expanded Perlite Composite as Form-Stable Phase Change Material for Latent Heat Thermal Energy Storage. *Renew. Energy* **2008**, *33* (12), 2599–2605. https://doi.org/10.1016/j.renene.2008.02.024.

(37) Kuroiwa, T.; Kimura, K.; Aoki, Y.; Neves, M. A.; Sato, S.; Mukataka, S.; Kanazawa, A.; Ichikawa, S. Quantitative Evaluation of the Effects of Moisture Distribution on Enzyme-Induced Acylation of Trehalose in Reduced-Moisture Organic Media. *J. Food Res.* **2015**, *4* (5), p133. https://doi.org/10.5539/jfr.v4n5p133.

(38) Yuan, S.; Sun, X.; Pang, J.; Lollar, C.; Qin, J.-S.; Perry, Z.; Joseph, E.; Wang, X.; Fang, Y.; Bosch, M.; Sun, D.; Liu, D.; Zhou, H.-C. PCN-250 under Pressure: Sequential Phase Transformation and the Implications for MOF Densification. *Joule* **2017**, *1* (4), 806–815. https://doi.org/10.1016/j.joule.2017.09.001.

(39) Kirchon, A.; Day, G. S.; Fang, Y.; Banerjee, S.; Ozdemir, O. K.; Zhou, H.-C. Suspension Processing of Microporous Metal-Organic Frameworks: A Scalable Route to High-Quality Adsorbents. *iScience* **2018**, *5*, 30–37. https://doi.org/10.1016/j.isci.2018.06.009.

(40) Vellingiri, K.; Szulejko, J. E.; Kumar, P.; Kwon, E. E.; Kim, K.-H.; Deep, A.; Boukhvalov, D. W.; Brown, R. J. C. Metal Organic Frameworks as Sorption Media for Volatile and Semi-Volatile Organic Compounds at Ambient Conditions. *Sci. Rep.* **2016**, *6*, 27813. https://doi.org/10.1038/srep27813.

(41) Vlasova, E. A.; Yakimov, S. A.; Naidenko, E. V.; Kudrik, E. V.; Makarov, S. V. Application of Metal–Organic Frameworks for Purification of Vegetable Oils. *Food Chem.* **2016**, *190*, 103–109. https://doi.org/10.1016/j.foodchem.2015.05.078.

(42) Kordas, A.; Magoulas, K.; Stamataki, S.; Tassios, D. Methane□hydrocarbon Interaction Parameters Correlation for the Peng-Robinson and the t-MPR Equation of State. *Fluid Phase Equilibria* **1995**, *112* (1), 33–44. https://doi.org/10.1016/0378-3812(95)02787-F.

(43) Choi, K. M.; Jeon, H. J.; Kang, J. K.; Yaghi, O. M. Heterogeneity within Order in Crystals of a Porous Metal–Organic Framework. *J. Am. Chem. Soc.* **2011**, *133* (31), 11920–11923. https://doi.org/10.1021/ja204818q.

(44) Wang, Z.; Hu, S.; Yang, J.; Liang, A.; Li, Y.; Zhuang, Q.; Gu, J. Nanoscale Zr-Based MOFs with Tailorable Size and Introduced Mesopore for Protein Delivery. *Adv. Funct. Mater.* **2018**, *28* (16), 1707356. https://doi.org/10.1002/adfm.201707356.

(45) Liu, W.; Huang, J.; Yang, Q.; Wang, S.; Sun, X.; Zhang, W.; Liu, J.; Huo, F. Multi-Shelled Hollow Metal–Organic Frameworks. *Angew. Chem.* **2017**, *129* (20), 5604–5608. https://doi.org/10.1002/ange.201701604.

(46) He, S.; Chen, Y.; Zhang, Z.; Ni, B.; He, W.; Wang, X. Competitive Coordination Strategy for the Synthesis of Hierarchical-Pore Metal–Organic Framework Nanostructures. *Chem. Sci.* **2016**, *7* (12), 7101–7105. https://doi.org/10.1039/C6SC02272C.

(47) Koo, J.; Hwang, I.-C.; Yu, X.; Saha, S.; Kim, Y.; Kim, K. Hollowing out MOFs: Hierarchical Micro- and Mesoporous MOFs with Tailorable Porosity via Selective Acid Etching. *Chem. Sci.* **2017**, *8* (10), 6799–6803. https://doi.org/10.1039/C7SC02886E.

(48) Diffenbaugh, N. S.; Singh, D.; Mankin, J. S.; Horton, D. E.; Swain, D. L.; Touma, D.; Charland, A.; Liu, Y.; Haugen, M.; Tsiang, M.; Rajaratnam, B. Quantifying the Influence of Global Warming on Unprecedented Extreme Climate Events. *Proc. Natl. Acad. Sci.* **2017**, *114* (19), 4881–4886. https://doi.org/10.1073/pnas.1618082114.

(49) Woodward, A. J.; Samet, J. M. Climate Change, Hurricanes, and Health. *Am. J. Public Health* **2017**, *108* (1), 33–35. https://doi.org/10.2105/AJPH.2017.304197.

(50) Hsiang, S.; Kopp, R.; Jina, A.; Rising, J.; Delgado, M.; Mohan, S.; Rasmussen, D. J.; Muir-Wood, R.; Wilson, P.; Oppenheimer, M.; Larsen, K.; Houser, T. Estimating

Economic Damage from Climate Change in the United States. *Science* **2017**, *356* (6345), 1362–1369. https://doi.org/10.1126/science.aal4369.

(51) Ahn, J.; Brook, E. J.; Mitchell, L.; Rosen, J.; McConnell, J. R.; Taylor, K.; Etheridge, D.; Rubino, M. Atmospheric CO2 over the Last 1000 Years: A High-Resolution Record from the West Antarctic Ice Sheet (WAIS) Divide Ice Core. *Glob. Biogeochem. Cycles* **2012**, *26* (2). https://doi.org/10.1029/2011GB004247.

(52) Friščić, T. New Opportunities for Materials Synthesis Using Mechanochemistry. *J. Mater. Chem.* **2010**, *20* (36), 7599–7605. https://doi.org/10.1039/C0JM00872A.

(53) Klimakow, M.; Klobes, P.; Thünemann, A. F.; Rademann, K.; Emmerling, F. Mechanochemical Synthesis of Metal−Organic Frameworks: A Fast and Facile Approach toward Quantitative Yields and High Specific Surface Areas. *Chem. Mater.* **2010**, *22* (18), 5216–5221. https://doi.org/10.1021/cm1012119.

(54) Luis, P. Use of Monoethanolamine (MEA) for CO2 Capture in a Global Scenario: Consequences and Alternatives. *Desalination* **2016**, *380*, 93–99. https://doi.org/10.1016/j.desal.2015.08.004.

(55) Yang, W.-C.; Hoffman, J. Exploratory Design Study on Reactor Configurations for Carbon Dioxide Capture from Conventional Power Plants Employing Regenerable Solid Sorbents. *Ind. Eng. Chem. Res.* **2009**, *48* (1), 341–351. https://doi.org/10.1021/ie800172e.

(56) Milner, P. J.; Siegelman, R. L.; Forse, A. C.; Gonzalez, M. I.; Runčevski, T.; Martell, J. D.; Reimer, J. A.; Long, J. R. A Diaminopropane-Appended Metal–Organic Framework Enabling Efficient CO2 Capture from Coal Flue Gas via a Mixed

Adsorption Mechanism. *J. Am. Chem. Soc.* **2017**, *139* (38), 13541–13553. https://doi.org/10.1021/jacs.7b07612.

(57) Nijem, N.; Thissen, P.; Yao, Y.; Longo, R. C.; Roodenko, K.; Wu, H.; Zhao, Y.; Cho, K.; Li, J.; Langreth, D. C.; Chabal, Y. J. Understanding the Preferential Adsorption of CO2 over N2 in a Flexible Metal–Organic Framework. *J. Am. Chem. Soc.* **2011**, *133* (32), 12849–12857. https://doi.org/10.1021/ja2051149.

(58) Kong, Y.; Jiang, G.; Fan, M.; Shen, X.; Cui, S.; Russell, A. G. A New Aerogel Based CO2 Adsorbent Developed Using a Simple Sol–Gel Method along with Supercritical Drying. *Chem. Commun.* **2014**, *50* (81), 12158–12161. https://doi.org/10.1039/C4CC06424K.

(59) Wang, X.; Li, H.; Liu, H.; Hou, X. AS-Synthesized Mesoporous Silica MSU-1 Modified with Tetraethylenepentamine for CO2 Adsorption. *Microporous Mesoporous Mater.* **2011**, *142* (2), 564–569. https://doi.org/10.1016/j.micromeso.2010.12.047.

(60) Liang, J.; Liang, Z.; Zou, R.; Zhao, Y. Heterogeneous Catalysis in Zeolites, Mesoporous Silica, and Metal–Organic Frameworks. *Adv. Mater.* **2017**, *29* (30), 1701139. https://doi.org/10.1002/adma.201701139.

(61) Siriwardane, R. V.; Shen, M.-S.; Fisher, E. P.; Losch, J. Adsorption of CO2 on Zeolites at Moderate Temperatures. *Energy Fuels* **2005**, *19* (3), 1153–1159. https://doi.org/10.1021/ef040059h.

(62) Cui, Y.; Du, J.; Liu, Y.; Yu, Y.; Wang, S.; Pang, H.; Liang, Z.; Yu, J. Design and Synthesis of a Multifunctional Porous N-Rich Polymer Containing s-Triazine and

Tröger's Base for CO2 Adsorption, Catalysis and Sensing. *Polym. Chem.* **2018**, *9* (19), 2643–2649. https://doi.org/10.1039/C8PY00177D.

(63) Huang, N.; Day, G.; Yang, X.; Drake, H.; Zhou, H.-C. Engineering Porous Organic Polymers for Carbon Dioxide Capture. *Sci. China Chem.* **2017**, *60* (8), 1007–1014. https://doi.org/10.1007/s11426-017-9084-7.

(64) Kim, I.; Svendsen, H. F. Heat of Absorption of Carbon Dioxide (CO2) in Monoethanolamine (MEA) and 2-(Aminoethyl)Ethanolamine (AEEA) Solutions. *Ind. Eng. Chem. Res.* **2007**, *46* (17), 5803–5809. https://doi.org/10.1021/ie0616489.

(65) Li, H.; Wang, K.; Feng, D.; Chen, Y.-P.; Verdegaal, W.; Zhou, H.-C. Incorporation of Alkylamine into Metal–Organic Frameworks through a Brønsted Acid–Base Reaction for CO2 Capture. *ChemSusChem* **2016**, *9* (19), 2832–2840. https://doi.org/10.1002/cssc.201600768.

(66) Lu, W.; Sculley, J. P.; Yuan, D.; Krishna, R.; Wei, Z.; Zhou, H.-C. Polyamine-Tethered Porous Polymer Networks for Carbon Dioxide Capture from Flue Gas. *Angew. Chem. Int. Ed.* **2012**, *51* (30), 7480–7484. https://doi.org/10.1002/anie.201202176.

(67) Quang, D. V.; Soukri, M.; Tanthana, J.; Sharma, P.; Nelson, T. O.; Lail, M.; Coleman, L. J. I.; Abu-Zahra, M. R. M. Investigation of CO2 Adsorption Performance and Fluidization Behavior of Mesoporous Silica Supported Polyethyleneimine. *Powder Technol.* **2016**, *301*, 449–462. https://doi.org/10.1016/j.powtec.2016.06.027.

(68) Zhu, X.; Do-Thanh, C.-L.; Murdock, C. R.; Nelson, K. M.; Tian, C.; Brown, S.; Mahurin, S. M.; Jenkins, D. M.; Hu, J.; Zhao, B.; Liu, H.; Dai, S. Efficient CO2 Capture

by a 3D Porous Polymer Derived from Tröger's Base. *ACS Macro Lett.* **2013**, *2* (8), 660–663. https://doi.org/10.1021/mz4003485.

(69) Lu, W.; Bosch, M.; Yuan, D.; Zhou, H.-C. Cost-Effective Synthesis of Amine-Tethered Porous Materials for Carbon Capture. *ChemSusChem* **2015**, *8* (3), 433–438. https://doi.org/10.1002/cssc.201402622.

(70) Tan, M. X.; Zhang, Y.; Ying, J. Y. Mesoporous Poly(Melamine–Formaldehyde) Solid Sorbent for Carbon Dioxide Capture. *ChemSusChem* **2013**, *6* (7), 1186–1190. https://doi.org/10.1002/cssc.201300107.

(71) Li, T.; Liang, J.; Cao, M.; Guo, X.; Xie, X.; Du, G. Re-Elucidation of the Acid-Catalyzed Urea–Formaldehyde Reactions: A Theoretical and 13C-NMR Study. *J. Appl. Polym. Sci.* **2016**, *133* (48). https://doi.org/10.1002/app.44339.

(72) Sangeetha, V.; Kanagathara, N.; Sumathi, R.; Sivakumar, N.; Anbalagan, G. Spectral and Thermal Degradation of Melamine Cyanurate https://www.hindawi.com/journals/jma/2013/262094/ (accessed Apr 25, 2020). https://doi.org/10.1155/2013/262094.

(73) Banerjee, R.; Phan, A.; Wang, B.; Knobler, C.; Furukawa, H.; O'Keeffe, M.; Yaghi, O. M. High-Throughput Synthesis of Zeolitic Imidazolate Frameworks and Application to CO2 Capture. *Science* **2008**, *319* (5865), 939–943. https://doi.org/10.1126/science.1152516.

(74) Sayari, A.; Belmabkhout, Y. Stabilization of Amine-Containing CO2 Adsorbents: Dramatic Effect of Water Vapor. *J. Am. Chem. Soc.* **2010**, *132* (18), 6312–6314. https://doi.org/10.1021/ja1013773.

(75) MOFs - Metal Organic Frameworks (MOFs) | Sigma-Aldrich https://www.sigmaaldrich.com/materials-science/material-science-products.html?TablePage=103996366 (accessed Apr 29, 2020).

(76) Lauby-Secretan, B.; Loomis, D.; Grosse, Y.; El Ghissassi, F.; Bouvard, V.; Benbrahim-Tallaa, L.; Guha, N.; Baan, R.; Mattock, H.; Straif, K.; WHO International Agency for Research on Cancer. Carcinogenicity of Polychlorinated Biphenyls and Polybrominated Biphenyls. *Lancet Oncol.* **2013**, *14* (4), 287–288. https://doi.org/10.1016/S1470-2045(13)70104-9.

(77) Borja, J.; Taleon, D. M.; Auresenia, J.; Gallardo, S. Polychlorinated Biphenyls and Their Biodegradation. *Process Biochem.* **2005**, *40* (6), 1999–2013. https://doi.org/10.1016/j.procbio.2004.08.006.

(78) Safe, S.; Hutzinger, O. Polychlorinated Biphenyls (PCBs) and Polybrominated Biphenyls (PBBs): Biochemistry, Toxicology, and Mechanism of Action. *CRC Crit. Rev. Toxicol.* **1984**, *13* (4), 319–395. https://doi.org/10.3109/10408448409023762.

(79) Birnbaum Linda S; Staskal Daniele F. Brominated Flame Retardants: Cause for Concern? *Environ. Health Perspect.* **2004**, *112* (1), 9–17. https://doi.org/10.1289/ehp.6559.

(80) Rahman, F.; Langford, K. H.; Scrimshaw, M. D.; Lester, J. N. Polybrominated Diphenyl Ether (PBDE) Flame Retardants. *Sci. Total Environ.* **2001**, *275* (1), 1–17. https://doi.org/10.1016/S0048-9697(01)00852-X.

(81) de Wit, C. A. An Overview of Brominated Flame Retardants in the Environment. *Chemosphere* **2002**, *46* (5), 583–624. https://doi.org/10.1016/S0045-6535(01)00225-9.

(82) Darnerud, P. O. Toxic Effects of Brominated Flame Retardants in Man and in Wildlife. *Environ. Int.* **2003**, *29* (6), 841–853. https://doi.org/10.1016/S0160-4120(03)00107-7.

(83) van der Veen, I.; de Boer, J. Phosphorus Flame Retardants: Properties, Production, Environmental Occurrence, Toxicity and Analysis. *Chemosphere* **2012**, *88* (10), 1119–1153. https://doi.org/10.1016/j.chemosphere.2012.03.067.

(84) Alongi, J.; Colleoni, C.; Rosace, G.; Malucelli, G. Phosphorus- and Nitrogen-Doped Silica Coatings for Enhancing the Flame Retardancy of Cotton: Synergisms or Additive Effects? *Polym. Degrad. Stab.* **2013**, *98* (2), 579–589. https://doi.org/10.1016/j.polymdegradstab.2012.11.017.

(85) Laoutid, F.; Bonnaud, L.; Alexandre, M.; Lopez-Cuesta, J.-M.; Dubois, Ph. New Prospects in Flame Retardant Polymer Materials: From Fundamentals to Nanocomposites. *Mater. Sci. Eng. R Rep.* **2009**, *63* (3), 100–125. https://doi.org/10.1016/j.mser.2008.09.002.

(86) Arao, Y. Flame Retardancy of Polymer Nanocomposite. In *Flame Retardants: Polymer Blends, Composites and Nanocomposites*; Visakh, P. M., Arao, Y., Eds.; Engineering Materials; Springer International Publishing: Cham, 2015; pp 15–44. https://doi.org/10.1007/978-3-319-03467-6_2.

(87) Morgan, A. B. A Review of Transition Metal-Based Flame Retardants: Transition Metal Oxide/Salts, and Complexes. In *Fire and Polymers V*; Wilkie, C. A., Morgan, A. B., Nelson, G. L., Eds.; ACS Symposium Series; American Chemical

Society: Washington, DC, 2009; Vol. 1013, pp 312–328. https://doi.org/10.1021/bk-2009-1013.ch019.

(88) Hou, Y.; Hu, W.; Gui, Z.; Hu, Y. A Novel Co(II)–Based Metal-Organic Framework with Phosphorus-Containing Structure: Build for Enhancing Fire Safety of Epoxy. *Compos. Sci. Technol.* **2017**, *152*, 231–242. https://doi.org/10.1016/j.compscitech.2017.08.032.

(89) Hou, Y.; Liu, L.; Qiu, S.; Zhou, X.; Gui, Z.; Hu, Y. DOPO-Modified Two-Dimensional Co-Based Metal–Organic Framework: Preparation and Application for Enhancing Fire Safety of Poly(Lactic Acid). *ACS Appl. Mater. Interfaces* **2018**, *10* (9), 8274–8286. https://doi.org/10.1021/acsami.7b19395.

(90) Zhao, Y.; Zhang, Q.; Li, Y.; Zhang, R.; Lu, G. Large-Scale Synthesis of Monodisperse UiO-66 Crystals with Tunable Sizes and Missing Linker Defects via Acid/Base Co-Modulation. *ACS Appl. Mater. Interfaces* **2017**, *9* (17), 15079–15085. https://doi.org/10.1021/acsami.7b02887.

(91) Katz, M. J.; Brown, Z. J.; Colón, Y. J.; Siu, P. W.; Scheidt, K. A.; Snurr, R. Q.; Hupp, J. T.; Farha, O. K. A Facile Synthesis of UiO-66, UiO-67 and Their Derivatives. *Chem. Commun.* **2013**, *49* (82), 9449. https://doi.org/10.1039/c3cc46105j.

(92) Barton, D.; Hodgett, M.; Skirving, P.; Whelton, M.; Winter, K.; Vardy, C. The Thermal Decomposition of Azobenzene. *Can. J. Chem.* **1983**, *61* (8), 1712–1718. https://doi.org/10.1139/v83-292.

(93) Korobeinichev, O. P.; Paletsky, A. A.; Gonchikzhapov, M. B.; Glaznev, R. K.; Gerasimov, I. E.; Naganovsky, Y. K.; Shundrina, I. K.; Snegirev, A. Yu.; Vinu, R.

Kinetics of Thermal Decomposition of PMMA at Different Heating Rates and in a Wide Temperature Range. *Thermochim. Acta* **2019**, *671*, 17–25. https://doi.org/10.1016/j.tca.2018.10.019.

(94) Hirata, T.; Kashiwagi, T.; Brown, J. E. Thermal and Oxidative Degradation of Poly(Methyl Methacrylate): Weight Loss. *Macromolecules* **1985**, *18* (7), 1410–1418. https://doi.org/10.1021/ma00149a010.

(95) Gałka, P.; Kowalonek, J.; Kaczmarek, H. Thermogravimetric Analysis of Thermal Stability of Poly(Methyl Methacrylate) Films Modified with Photoinitiators. *J. Therm. Anal. Calorim.* **2014**, *115* (2), 1387–1394. https://doi.org/10.1007/s10973-013-3446-z.

(96) Shen, R.; Hatanaka, L. C.; Ahmed, L.; Agnew, R. J.; Mannan, M. S.; Wang, Q. Cone Calorimeter Analysis of Flame Retardant Poly (Methyl Methacrylate)-Silica Nanocomposites. *J. Therm. Anal. Calorim.* **2017**, *128* (3), 1443–1451. https://doi.org/10.1007/s10973-016-6070-x.

(97) E05 Committee. *Test Method for Heat and Visible Smoke Release Rates for Materials and Products Using an Oxygen Consumption Calorimeter*; ASTM International. https://doi.org/10.1520/E1354-17.

(98) Fang, Y.; Banerjee, S.; Joseph, E. A.; Day, G. S.; Bosch, M.; Li, J.; Wang, Q.; Drake, H.; Ozdemir, O. K.; Ornstein, J. M.; Wang, Y.; Lu, T.-B.; Zhou, H.-C. Incorporating Heavy Alkanes in Metal–Organic Frameworks for Optimizing Adsorbed Natural Gas Capacity. *Chem. – Eur. J.* **2018**, *24* (64), 16977–16982. https://doi.org/10.1002/chem.201804012.

(99) Day, G. S.; Drake, H. F.; Joseph, E. A.; Bosch, M.; Tan, K.; Willman, J. A.; Carretier, V.; Perry, Z.; Burtner, W.; Banerjee, S.; Ozdemir, O. K.; Zhou, H.-C. Improving Alkylamine Incorporation in Porous Polymer Networks through Dopant Incorporation. *Adv. Sustain. Syst.* **2019**, *3* (12), 1900051. https://doi.org/10.1002/adsu.201900051.